A&A, 710, A214 (2026)
https://doi.org/10.1051/0004-6361/202556741

Astronomy & Astrophysics

Mapping the emission and spectral properties of the FRI radio galaxy 3C 449 with LOFAR and the VLA

Luca Ricci[1,2,3,⋆], Luisa Ostorero[3,4,5], Raffaella Morganti[6,7], Judith H. Croston[8], Martin J. Hardcastle[9], and Timothy W. Shimwell[6,10]

[1] Julius-Maximilians-Universität Würzburg, Fakultät für Physik und Astronomie, Institut für Theoretische Physik und Astrophysik, Lehrstuhl für Astronomie, Emil-Fischer-Str. 31, D-97074 Würzburg, Germany
[2] Max-Planck-Institut für Radioastronomie, Auf dem Hügel, 69, D-53121 Bonn, Germany
[3] Dipartimento di Fisica, Universitá di Torino, Via P. Giuria 1, I-10125 Torino, Italy
[4] Istituto Nazionale di Fisica Nucleare (INFN), Sezione di Torino, Via P. Giuria 1, I-10125 Torino, Italy
[5] INAF – Osservatorio Astrofisico di Torino, Via Osservatorio 20, I-10025 Pino Torinese, Italy
[6] ASTRON, the Netherlands Institute for Radio Astronomy, Oude Hoogeveensedijk 4, 7991 PD Dwingeloo, The Netherlands
[7] Kapteyn Astronomical Institute, University of Groningen, Postbus 800, 9700 AV Groningen, The Netherlands
[8] School of Physical Sciences, Open University, Walton Hall MK7 6AA, UK
[9] Centre for Astrophysics Research, University of Hertfordshire, College Lane, Hatfield AL10 9AB, UK
[10] Leiden Observatory, Leiden University, PO Box 9513, 2300 RA Leiden, The Netherlands

Received 4 August 2025 / Accepted 13 April 2026

ABSTRACT

The jets and lobes of nearby, extended radio galaxies are ideal laboratories for exploring the spectral and dynamical evolution of the radio emitting plasma that emanates from active galactic nuclei and propagates through the ambient medium. Here, we present a deep, high-resolution radio continuum study of the low-redshift ($z = 0.01713$), Fanaroff-Riley class I (FRI) radio galaxy 3C 449 performed with a combination of radio data at 145 MHz acquired with the LOw Frequency ARray (LOFAR) and archival Very Large Array (VLA) data at 1365, 1485, 4985, and 8485 MHz. Our LOFAR maps of the source have angular resolution $20'' \times 20''$ ($7.2\,\mathrm{kpc} \times 7.2\,\mathrm{kpc}$) and $6.0'' \times 6.0''$ ($2.2\,\mathrm{kpc} \times 2.2\,\mathrm{kpc}$), revealing the full extent of the known radio emission ($\approx 22'$, i.e. ≈ 480 kpc) at the highest angular resolution achieved to date. Our spectral index maps show, for the first time, the high-resolution distribution of the spectrum in the 145–8485 MHz frequency range over a source region that extends beyond $2.5'$ (54 kpc). The average 145–8485 MHz source spectrum is consistent with a single power law and stays approximately constant over the inner $\approx 50''$ (≈ 18 kpc) of both source jets. Beyond $\approx 50''$, both on the northern and on the southern source sides, the higher-frequency spectrum steepens and the spectral break frequency lowers with increasing distance from the radio core, indicating the absence of relevant sites of particle acceleration beyond those distances. In our 145–1365 MHz spectral index map, we detected a flatter spectrum spine surrounded by a steeper spectrum sheath in the inner $\approx 2.5'$ (54 kpc) and $\approx 3'$ (65 kpc) of the southern and northern jet, respectively. Beyond $\approx 1'$, the spine-sheath structure was also detected in the 1365–8485 MHz frequency range, confirming previous findings. The steep spectrum sheath may be the signature of interaction between the jet and the ambient medium. By modelling the spectral index maps under the assumption of equipartition and of a constant magnetic field across the source, we derived maps of the highest radiative age of the particles all over the source in a standard ageing scenario. From the oldest radiating plasma, located in the southern radio lobe, we estimated the source spectral age as $\tau \simeq 200$ Myr. At the outer edges of both the northern tail and southern lobe, we estimated a spectral age of $\tau_{\mathrm{sp}} \simeq 150$ Myr. If the latter age were representative of the dynamical source age, the average expansion speed of both jets during the source lifetime would be supersonic, with $M \simeq 4.1$ and $M \simeq 2.8$ for the northern and southern jets, respectively. Because numerical magneto-hydrodynamical simulations of FRI jets suggest that the source's current expansion is subsonic, the high average Mach numbers might arise either from the source being highly supersonic for a small fraction of its lifetime or from a severe underestimation of the spectral age. This is either due to particle acceleration on scales of hundreds of kiloparsecs (not detected in our observations) or to the presence of a non-homogeneous magnetic field with a complex structure.

Key words. galaxies: active – galaxies: individual: 3C 449 (B2 2229+39) – galaxies: jets – radio continuum: galaxies

1. Introduction

Radio galaxies that are extended on spatial scales of a few hundred kiloparsecs (kpc) or greater are thought to sample the evolved radio galaxy population. Based on their radio morphology, they can broadly be grouped into Fanaroff & Riley (1974) class I (FRI) and class II (FRII) objects, even though additional classifications have been introduced to account for hybrid morphology radio sources and sources without a straight radio structure (see e.g. Hardcastle & Croston 2020, for a recent review).

FRII sources are known as edge-brightened sources and their jets are thought to be highly relativistic out to large distances from the radio core. When detected, FRII jets mostly show a one-sided or two-sided, highly asymmetric structure that is found to terminate in a hot spot at their edges, which is the primary site of particle acceleration. Terminal hot spots can be detected on both sides even when only the approaching jet is visible (e.g. Mullin et al. 2006). Conversely, FRI sources are assumed to be edge-darkened (or centre brightened), possessing twin jets that dominate the surface brightness and diffuse plumes. The jets are thought to be launched with highly relativistic speeds; however,

⋆ Corresponding author: luca.ricci@unito.it

on kpc scales, they experience a deceleration to non-relativistic speeds (Laing & Bridle 2014), which might be the primary cause of particle acceleration (Laing & Bridle 2013) that has been directly observed in the inner parts of the jets through X-ray and optical synchrotron radiation.

The FRI-FRII dichotomy may be linked to jet dynamics. Originally, the FRI-FRII morphological divide was found to correspond to a radio luminosity break, $L_{150\,\mathrm{MHz}} \simeq 10^{26}\,\mathrm{W\,Hz^{-1}}$ (Fanaroff & Riley 1974), that appeared to increase with the luminosity of the host elliptical galaxy (Owen & Ledlow 1994; Ledlow & Owen 1996). This suggests that for a given radio luminosity, the distinction between FRI and FRII morphology might be a consequence of both the luminosity and the core density of galaxies, with the FRI morphology occurring in the denser cores of more optically luminous hosts (e.g. De Young 1993; Bicknell 1995; Mingo et al. 2019). As a result, FRI and FRII sources would clearly be different in the locations of particle acceleration and the particle contents on large scales (e.g. Croston et al. 2018). Even though recent studies have shown that the radio luminosities of FRIs and FRIIs span a wide range and display a significant overlap, it remains true that FRIIs are on average more luminous than FRIs (e.g. Clews et al. 2025, and references therein). In addition, despite the relation between radio luminosity and host luminosity (Ledlow & Owen 1996) disappearing when selection effects are properly accounted for, radio galaxies near the FR luminosity divide preferentially show FRI morphology if they are hosted by more massive galaxies, supporting evidence that the inner environment plays a role in determining jet disruption (Clews et al. 2025).

A possible additional, extrinsic cause of the FRI-FRII dichotomy is the large-scale environment of the host galaxies, with the inter-galactic medium (IGM) density standing as the differentiating factor in the resistance experienced by the jets (e.g. Prestage & Peacock 1988). Even though there is a significant overlap in environment between the two classes, FRI sources generally tend to be found in higher density environments, as compared to FRII sources (e.g. Zirbel 1997; Gendre et al. 2013; Croston et al. 2019). Finally, the role of the accretion mode, in turn linked to the large scale environment, as a supplementary, intrinsic cause in shaping the jet morphology, is still under debate (e.g. Best & Heckman 2012; Gendre et al. 2013; Mingo et al. 2014; Ineson et al. 2015; Tadhunter 2016; Hardcastle et al. 2007; Czerny & You 2016; Hardcastle 2018).

Despite the absence of a unique factor separating the FRI and FRII sources, the above evidence has long suggested that the characteristic features of FRI sources could be mostly ascribed to deceleration and disruption of their (typically lower power) jets by a denser surrounding medium, as originally proposed by Simon (1978). These processes might be triggered by mass entrainment via a mixing, turbulent layer at the jet surface (Bicknell 1984, 1986; De Young 1993; Laing & Bridle 2002a; Wang et al. 2009), promoted by various types of jet instabilities (e.g. Perucho et al. 2005; Perucho & Martí 2007; Meliani & Keppens 2007, 2009; Matsumoto & Masada 2013; Millas et al. 2017; Tchekhovskoy & Bromberg 2016; Rossi et al. 2020, 2024), by mass loading from stellar winds within the jet volume (Komissarov 1994), or by stars penetrating and exiting the jets and triggering instabilities that favour mixing (Perucho 2020). The efficiency of all these mechanisms is higher on galaxy scales.

As a consequence of the mass entrainment on galaxy scale, FRI jets develop a boundary layer (sheath) that transfers momentum to the ambient gas and propagates at lower speed than the central spine (e.g. Bicknell 1984, 1986; Rosen & Hardee 2000; Laing & Bridle 2002b). This spine-sheath structure may persist on larger scales, where the jet interacts with the ICM (e.g. Loken et al. 1995; Massaglia et al. 2019).

The role of the jet magnetic field might also be important for shaping the radio morphology, after the deceleration phase: three-dimensional, magneto-hydrodynamical (3D MHD) numerical simulations of the propagation of plasma jets in a stratified ambient medium (e.g. Massaglia et al. 2019, 2022) show that while low-power (high-power) jets lead to FRI (FRII) morphology radio galaxies, intermediate-power jets preferentially lead to FRI morphologies if they are highly magnetised.

Both the magnetic field distribution and the source substructures created by the jet-ambient interaction are expected to determine the surface brightness and spectral index distribution of a radio source. Indeed, in radio sources, energetic electrons are expected to be accelerated mostly by strong shocks inside the jet and its cocoon via diffusive shock acceleration – or the Fermi first-order process (Blandford & Ostriker 1978; Drury 1983; Blandford & Eichler 1987), although other microphysical processes, such as Fermi second-order acceleration and reconnection at shear layers (Rieger & Duffy 2007; Rieger et al. 2007; Sironi et al. 2021), might also be at work. After an acceleration event, the electrons are expected to suffer cooling due to synchrotron and inverse-Compton losses. Therefore, testing dynamical models of FRI sources against observations requires the availability of reliable simulations of the surface-brightness distribution and corresponding high resolution radio observations at different frequencies. In MHD simulations, the surface-brightness distribution is often inferred from the simulated density distribution and the pressure behaviour of the jets (e.g. Rosen & Hardee 2000; Massaglia et al. 2019, 2022). On the other hand, semi-analytical calculations can predict the evolution of the energy spectrum of non-thermal electron populations moving in a fluid flow (Kardashev 1962; Jaffe & Perola 1973; Murgia et al. 1999; Hardcastle 2013); however, this comes with simplifying assumptions. A more complete and self-consistent approach requires following the evolution of the population of relativistic radiating particles in 3D relativistic MHD (RMHD) numerical simulations of the source dynamics (Fromm et al. 2016; Turner et al. 2018; Vaidya et al. 2018; Davelaar et al. 2020; Mukherjee et al. 2021). Even though these simulations are still computationally very expensive, the first results on jets unstable to MHD instabilities, as may be the low-power jets of FRIs, show that the complex shock structures created by the jet-ambient interaction on scales of $\lesssim$10 kpc are indeed capable of accelerating particles (Mukherjee et al. 2021). These results are encouraging in showing the possibility to identify the main sites and mechanisms of particle acceleration, and, in the long run, to simultaneously follow the dynamical and spectral evolution of the full radio source.

The LOw Frequency ARray (LOFAR) Telescope (van Haarlem et al. 2013) is the ideal instrument for performing studies of the surface-brightness distribution of extended radio galaxies of the FRI type. With its ability to observe the sky at low frequencies, high sensitivity, and high angular resolution, LOFAR enables the imaging of the low-frequency emission of these sources in detail. The combination of LOFAR data with data at higher radio frequencies, such as those acquired with the Very Large Array (VLA), offers the unique opportunity to map the distribution of the spectral properties of these sources. In this context, we carried out a study of the radio continuum emission of the FR I radio galaxy 3C 449 (B2 2229+39). Thanks to the combination of its vicinity, luminosity, as well as apparent and intrinsic large size, this source is one of the best targets to

investigate the distribution of the surface brightness and spectral index on scales from few kpc up to hundreds of kpc.

3C 449 is an FRI radio galaxy (Fanaroff & Riley 1974; Perley et al. 1979; Pearson & Readhead 1988). It is hosted by the nearby (z = 0.01708; de Vaucouleurs et al. 1991) elliptical galaxy UGC 12064, which is the most prominent member, classified as cD by Wyndham (1966), of the poor galaxy cluster Zw 2231.2+3732. UGC 12064 has a bright, elliptical companion 37″ (13 kpc) in projection to the north; the haloes of the two galaxies are connected by a low-surface-brightness bridge (Martel et al. 1999). The source is not among those with confirmed synchrotron optical jets, according to Martel et al. (1999, see, however, Capetti et al. 1994).

From VLA observations at 1.4 GHz, the source appears to have a total extent of ≈20′ (≈430 kpc): two opposite jets start from an unresolved core and appear to be fairly symmetrical on scales of ≈1′ (≈21.6 kpc). They then merge into the inner lobes and subsequently follow a structure that resembles a helix in projection (Perley et al. 1979; Feretti et al. 1999). From dynamical studies, the jets were found to be almost aligned with the plane of the sky, with an angle to the line of sight of $\theta > 75°$ (Feretti et al. 1999). The radio source expands within a distribution of X-ray-emitting gas whose surface-brightness peak corresponds to the position of the radio core (Hardcastle et al. 1998; Croston et al. 2003; Lal et al. 2013). The high galaxy number density and X-ray gas density that characterise the environment of 3C 449 are consistent with its classification as an FRI radio galaxy. The hot gas distribution that embeds the source is not spherically symmetric, with the large-scale radio emission that avoids the regions of higher X-ray surface brightness. A tunnel-like feature and an X-ray cavity are detected in correspondence of the southern radio jet and inner lobe, respectively (Hardcastle et al. 1998; Croston et al. 2003; Sun et al. 2009; Lal et al. 2013). Even though the orbital motion of the two companion galaxies was initially proposed to be responsible for the wiggles of the jets (Lupton & Gott 1982; Hardee et al. 1994), the fact that both of the inner jets are bent to the west as they enter their respective lobes led Lal et al. (2013) to suggest that the ambient gas is rather pushing them westward; moreover, the inner jets flare at approximately the position of a 'sloshing' gas cold front ascribed to a group merger occurred $\lesssim$1.3−1.6 Gyr ago, suggesting that the jet is entraining and thermalising some of the hot gas as it crosses the front, as predicted by Loken et al. (1995).

The radio spectral properties of 3C 449 have been extensively studied by means of both single-dish and interferometric observations. Jaegers (1987) used early, moderate-angular-resolution (RA × DEC = 29″ × 46″) interferometric observations with the Westerbork Synthesis Radio Telescope at 608 MHz and 1400 MHz to show that the 600–1400 MHz spectrum progressively steepens with core distance out to ∼9′ in the north and out to ∼6′ in the south; a spectral flattening appears beyond ∼6′ in the southern lobe. With single-dish, low angular resolution (2.5′ and 4.5′) observations acquired with both the Bologna Northern Cross and Effelsberg radio telescopes at 400, 2700 and 4750 MHz, and 10.7 and 32 GHz, Andernach et al. (1992) showed that the spectrum progressively steepens with core distance out to >9′ in each pair of frequencies in the 400 MHz–10.7 GHz range, and out to ∼5′ at 10.7–32 GHz; some spectral flattening is observed at the southernmost edge of the source in the 400–2700 MHz range, consistently with the findings of Jaegers (1987). High-resolution interferometric observations were performed with the VLA by Perley et al. (1979) at 1465–4885 MHz with ∼4″ resolution, by Katz-Stone & Rudnick (1997) at 330, 1445, and 4835 MHz with ∼3.6″ resolution, and by Feretti et al. (1999) at 4985 and 8385 MHz with 1.25″−5″ resolution. The investigations by Katz-Stone & Rudnick (1997) and Feretti et al. (1999) showed that the radio spectrum is roughly constant, on both source sides, out to ≈1′ from the core, confirming earlier findings by Perley et al. (1979). Beyond 1′, the overall spectrum steepens with increasing distance from the core out to ≈2.5′, with an asymmetric behaviour on the two source sides, with the southern, inner lobe that appears to be steeper than the northern, inner lobe. While Katz-Stone & Rudnick (1997) found evidence, on both source sides, of a 'flat jet' whose spectrum remains roughly constant with the core distance, and a 'sheath' that appears beyond 1′ from the core and is responsible for the steepening of the overall spectrum with increasing core distance and for most of the observed source widening, Feretti et al. (1999) did not distinguish between flat jet and sheath for the northern part of the source, and only confirmed the separation between a flat jet and a surrounding, steeper region in the southern part of the source. The southern, steeper spectrum radio emitting sheath was more recently associated with the X-ray sheath around the X-ray tunnel by Lal et al. (2013). Both radio spectral studies by Katz-Stone & Rudnick (1997) and Feretti et al. (1999) are limited to within ≈2.5′ (≈54 kpc) from the core, namely to the source region within the inner lobes.

In this work, we present new LOFAR observations of 3C 449 at 145 MHz and we combine them with re-analysed archival VLA observations at 1365, 1485, 4985, and 8485 MHz, with the aim of obtaining, for the first time, high-resolution spectral index maps of the source that extend well beyond 2.5′[1]. We used these maps to look for signatures of particle acceleration processes occurring in the jets and lobes, to explore the interaction between expanding jet and ambient medium, to estimate the source spectral age and constrain the dynamics of the source expansion. The paper is organised as follows. In Sect. 2, we describe the LOFAR-HBA observations and the data reduction procedure, as well as the re-analysis of the VLA archival data. In Sect. 3, we present the source morphology as seen by LOFAR (Sect. 3.1), the maps of radio spectral index obtained from the combination of LOFAR and VLA maps, and the profiles of the spectral index along and across the radio structures (Sect. 3.2). In Sect. 4, we perform the spectral analysis: by modelling the combination of the surface-brightness images of the source at different frequencies, we map the spectral age of the radio emitting particles and infer the spectral age of the source. In Sect. 5 we discuss our results in terms of constraints to the source dynamics (Sect. 5.1) and of particle populations and acceleration mechanisms (Sect. 5.2). We present our conclusions in Sect. 6.

We adopted J2000.0 as the equinox of coordinates. We adopted a cosmological model that assumes a flat Universe with $\Omega_M = 0.308$ and $H_0 = 67.8\,\mathrm{km\,s^{-1}\,Mpc^{-1}}$ (Planck Collaboration XIII 2016). In this model, 1″ corresponds to 0.360 kpc at the source redshift of z = 0.01713.

2. Observations and data reduction

2.1. LOFAR HBA data

3C 449 was observed twice with the LOFAR high band antenna (HBA). The first observation was a dedicated ten-hour run on August 16, 2015 (project LC4_028; observation ID L368474; PI: V. Heesen), with the LOFAR telescope operating in the HBA_DUAL_INNER configuration, resulting in a field of view

[1] In this work, we did not use the 330 MHz VLA observations, due to their poor quality and, thus, the low S/N of the extended emission.

(FOV) of approximately 8° with baseline lengths of up to 85 km. The quality of the image obtained with this observation was not good enough to perform a spectral analysis, due to severe artifacts remaining after self-calibration; therefore, we will not discuss it further in this work.

The source was then observed as part of the ongoing LOFAR Two Meter Sky Survey (LoTSS; Shimwell et al. 2017, 2019, 2022) project and we used the pointing P337+38 observed on March 07, 2020. In this pointing, 3C 449 is located 1.10 degrees from the field centre. The observations were carried out with the standard LoTSS survey setup (Shimwell et al. 2019, 2022), i.e. 8 h on-source observations bookended on either side with a flux density calibrator, in this case 3C 295. The observation used 51 antennas (24 core, 14 remote, 13 international). The observations were recorded with an integration time of 1 s, a 48 MHz bandwidth centred at 144.6 MHz and a channel width of 3.05 kHz. The details of this observation are reported in Table 1. The data from the international stations, although recorded, are not used in the present paper. Full details of the observational setup and processing of these data are given as part of the LoTSS DR3 release (Shimwell et al. 2026).

The data were passed through the standard LOFAR preprocessing pipeline (Heald et al. 2010) which performed the flagging of the radio frequency interference (RFI) using the AOflagger (Offringa et al. 2012) and averaged down to a channel width of 12.2 kHz. A direction-independent calibration was then performed using the PREFACTOR1 pipeline (de Gasperin et al. 2019; van Weeren et al. 2016; Williams et al. 2016).

The output datasets were then processed with DDF pipeline[2], which performs direction dependent (DD) calibration and imaging. This pipeline makes use of kMS and DDFacet for calibration and imaging, respectively. The processing was performed as part of the standard LoTSS-DR3 processing and uses v3.0 of DDF-pipeline. DDF pipeline is described in detail in Tasse et al. (2021) and Shimwell et al. (2022).

For the analysis presented in this paper, we used images of the field at both $6'' \times 6''$ and $20.0'' \times 20.0''$ resolution to trace the faint large-scale emission, while also having the ability to map the details in the large-scale structure. The images at both resolutions are shown in Fig. 2 and their characteristics are listed in Table 2.

The flux density scale by Scaife & Heald (2012) is used for the calibration of the calibrator source in PREFACTOR1 and TGSS-ADR1 sky models of the target fields are used for an initial phase calibration. However, density scale errors arise when transferring the calibration solutions to the target field (possibly related to uncertainties in the LOFAR beam model and the differing elevations of the target and calibrator fields); for this reason, in LoTSS, the flux density scale of the target field is further refined during processing. This is done by deriving a scaling factor to match the flux density scale with that of NVSS (Hardcastle et al. 2016). For this field, a flux scaling factor of 1.161 was applied. In addition, the error associated with the measured flux densities is dominated by the flux calibration uncertainty, that is typically assumed to be between 10% and 20% (Shimwell et al. 2022), and that we evaluated to be ≃14% (see Sect. 2.4 for details).

2.2. VLA data

We retrieved archival Very Large Array (VLA) data of 3C 449 acquired by Katz-Stone & Rudnick (1997) at 1365 MHz, 1485 MHz, 4895 MHz and 8485 MHz (i.e. in the *L*, *C*, and *X* bands), and by Feretti et al. (1999) at 8485 MHz (i.e. in the *X* band). The details of the VLA data sets are reported in Table 3. We reprocessed the data using the Common Astronomy Software Applications (CASA) package. After the online flagging, the data were manually flagged and calibrated using the flux scale of Perley & Butler (2013), which is consistent with the scale of Scaife & Heald (2012) at low frequencies (30–300 MHz). Phase self-calibration runs were performed for each map. A single amplitude self-calibration run was performed when needed. The primary beam correction was applied to all the VLA images. The flux calibrators were 3C 286 and 3C 48, which are unresolved at the resolution of our observations. The phase calibrator was the nearby source 2200+420.

The combination of VLA and LOFAR maps to study the spatial distribution of the source radio spectral index requires the same angular resolution for the combined maps. To obtain VLA maps that match the angular resolution of the LOFAR maps at 145 MHz (i.e. $6.0'' \times 6.0''$ and $20'' \times 20''$) as much as possible without applying a heavy smoothing of the beam, we proceeded as follows. We first combined data acquired in different VLA configurations (see Table 3, entry no. 4); subsequently, to achieve exactly the same angular resolutions of the LOFAR images, we restored each pair of maps to have the same (u, v)-coverage[3] and then restored the VLA images using the `restoringbeam` command during the imaging process. As the short baselines are crucial to recover the extended emission, for each pair of images, the (u, v)-range was cut to the shortest common baseline to produce accurate spectral index maps. Our procedure is similar to the procedure followed by Heesen et al. (2018) to combine LOFAR and VLA data of 3C 31. Our re-analysed VLA maps are displayed in Appendix B.

Table 1. LOFAR HBA observations.

LoTSS project code	P337+38
Central frequency	144.627 MHz
Bandwidth	48 MHz (120–168 MHz)
Time on source	8 h
Flux calibrator	3C 295
Observation date	2020-03-07

2.3. General map properties

A summary of the characteristics of the LOFAR and VLA maps is reported in Table 2, which lists the observation frequencies, the array configuration used for the VLA, the angular resolution of the maps, the calibrators, and the map rms noise level.

At high resolution (i.e. $6.0'' \times 6.0''$), the quality of our reprocessed VLA images is comparable to the quality of the original images presented in Katz-Stone & Rudnick (1997) and in Feretti et al. (1999). For example, Feretti et al. (1999) achieved rms noise levels, $\sigma_{\rm rms}$, of 0.035 mJy beam^{-1} at 1365 MHz, 0.018 mJy beam^{-1} at 4985 MHz, and 0.011 mJy beam^{-1} at 8485 MHz, comparable to our rms noise levels, listed in Table 2. Furthermore, Feretti et al. (1999) estimated core flux densities of 37.0 mJy at 5 GHz and 45.0 mJy at 8.4 GHz, both with observations in the C configuration. These values are consistent with our core flux densities of 38.0 ± 0.8 mJy 44.0 ± 0.9 mJy, respectively.

[2] https://github.com/mhardcastle/ddf-pipeline

[3] We also produced the spectral index maps without restricting them to the same (u, v)-coverage and no important differences were seen.

Table 2. Characteristics of the LOFAR and VLA maps obtained and re-obtained, respectively, in this work.

Telescope	Frequency (MHz)	Configuration (VLA)	Calibrators (flux, phase)	Angular resolution (arcsec)	rms noise (mJy beam^{-1})
LOFAR	145	//	...	$6.0'' \times 6.0''$	0.142
LOFAR	145	//	...	$20.0'' \times 20.0''$	0.214
VLA	1365	B,C,D	3C 286, 2200+420	$6.0'' \times 6.0''$	0.038
VLA	1365	C,D	3C 286, 2200+420	$20.0'' \times 20.0''$	0.030
VLA	1485	B,D	3C 286, 2200+420	$20.0'' \times 20.0''$	0.054
VLA	4985	C,D	3C 286, 2200+420	$6.0'' \times 6.0''$	0.016
VLA	8485	C,D	3C 286, 2200+420	$6.0'' \times 6.0''$	0.018

Notes. Column 1: array used for the observation; Column 2: frequency in MHz of the observation; Column 3: VLA configuration used; Column 4: flux and phase calibrators used for the data reduction; Column 5: angular resolution of the final image in arcsec; Column 6: thermal noise of the final image in mJy beam^{-1}.

Katz-Stone & Rudnick (1997) reported a surface brightness of 18.42 mJy beam^{-1} for the core region at 20 cm, comparable to our estimate of 23.45 mJy beam^{-1}. The slightly higher core surface brightness in our VLA images is likely due to the fact that our beam ($6.0'' \times 6.0''$) is larger than theirs ($3.6'' \times 3.6''$). At low resolution (i.e. $20'' \times 20''$), the quality of our maps in the L band (i.e. at 1365 and 1485 MHz) is comparable to their higher angular resolution counterparts.

2.4. Flux scale and uncertainties

Studying the spectral properties of the radio emission requires an accurate flux density scale. In LoTSS-DR2, the systematic overall flux density scale error is less than 10%, but there is a further up to 10% random error; both of these errors vary across the sky. Assuming these errors are independent, we added them in quadrature to give an error of ≃14% to the flux density scale error.

To further check the accuracy of the flux density scale of our LOFAR image of 3C 449, we assembled the radio spectrum of 3C 449 by combining the integrated flux densities of the source that we derived from the LOFAR and VLA maps analysed in this work with the flux densities taken from the literature. In our images, the integrated flux densities were measured by using $3\sigma_{\rm rms}$ contours as reference.

The total uncertainties on the LOFAR and VLA flux densities derived in this work were computed by combining in quadrature the rms noise, averaged over an area of 10 beams, and the flux density scale error. The 10-beam areas considered for the rms noise were outside the radio source and did not show any artifact. We considered the uncertainty on the flux density scale to be the above-mentioned 14% for the LOFAR maps (Shimwell et al. 2022) and 2% for the VLA maps (Perley & Butler 2013). For both LOFAR and VLA observations, the flux density scale uncertainty is the dominant error. The rms noise uncertainty is always $\sigma_{\rm rms} \sim 10^{-4}$ Jy.

Figure 1 shows the integrated radio spectrum of 3C 449 in the frequency range 86–8485 MHz. The values of the integrated flux densities and their uncertainties are reported in Appendix A. Assuming that the radio spectrum is described by a power law of the form $S_\nu = K\nu^{-\alpha}$, we fitted a straight line, that takes the form $\log S_\nu = \log K - \alpha \log \nu$, to the logarithmic spectrum, without including the LOFAR points in the analysis. The regression line, represented with a solid, black line in Fig. 1, has the following parameters: $\alpha = 0.76 \pm 0.03$ and $\log K = 795 \pm 169$. The black, dotted lines in Fig. 1 enclose the range of variation of the best fit according to the 1σ uncertainties on the best-fit parameters. The integrated flux densities at 145 MHz derived from the LOFAR maps are consistent with the flux density at 145 MHz expected for a single power-law spectrum at the 1σ level.

Table 3. VLA data reprocessed in this work.

Observation ID	AK0319	AF0241
Bands	L, C, X	X
Frequency (MHz)	(a) 1365	8485
	(b) 1485	
	(c) 4985	
	(d) 8485	
VLA configurations	B, C, D	C
Observation time (h)	(a) 5.2 (B), 1.0 (C) 0.6 (D)	5.5 (C)
	(b) 5.2 (B), 0.6 (D)	
	(c) 8.7 (C), 1.8 (D)	
	(d) 1.8 (D)	
Primary calibrators	3C 286	3C 286
	3C 48	
Secondary calibrator	2200+420	2200+420
Observation dates	1993/04–1994/01	1993/07

3. Morphology and spectral index distribution

3.1. Morphology

Our two LOFAR maps, displayed in Fig. 2, show the source morphology at 145 MHz at the different angular resolutions listed in Table 2. The map in the left panel has a resolution of $6.0'' \times 6.0''$ (2.2 kpc × 2.2 kpc), while the map in the right panel has a resolution of $20.0'' \times 20.0''$ (7.2 kpc × 7.2 kpc). For ease of description of the results and comparison with the literature, in Fig. 2 we label the different regions of the radio source as in Feretti et al. (1999).

In our LOFAR maps, the source has a total extension out to 3σ of 22.2′ (479.5 kpc) at $6.0'' \times 6.0''$ resolution, and of 22.3′ (481.7 kpc) at $20.0'' \times 20.0''$ resolution. For comparison, our reanalysed VLA maps at $6.0'' \times 6.0''$ resolution show a source full extension of ≈22′ at 1365 MHz, ≈11′ at 4985 MHz, and ≈7′ at 8485 MHz, whereas the maps at $20.0'' \times 20.0''$ resolution have a total extension of ≈20′ at 1365 MHz and ≈22′ at 1485 MHz.

Thanks to the combination of low frequency and high sensitivity, our higher angular resolution ($6.0'' \times 6.0''$) LOFAR map reveals additional, faint emission previously undetected by the VLA map at 1365 MHz with the same angular resolution (see

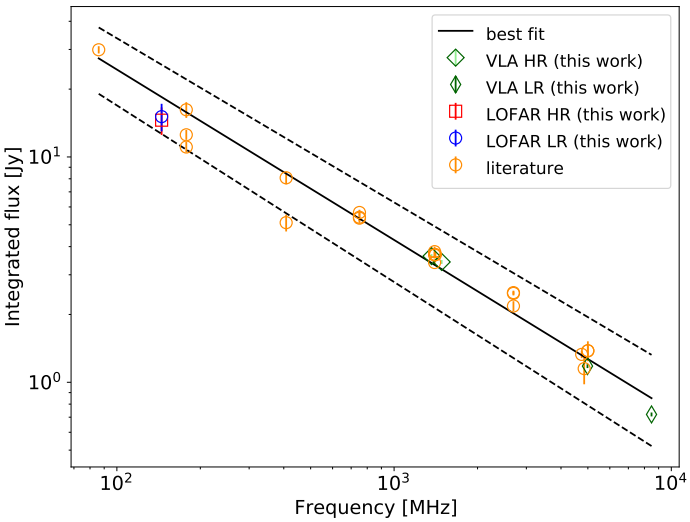

Fig. 1. Integrated radio spectrum of 3C 449 in the frequency range 86–8485 MHz. Symbols are as follows. Red square: 145 MHz flux density derived from the LOFAR map at 6.0″ × 6.0″; blue circle: 145 MHz flux density derived from the LOFAR map at 20.0″ × 20.0″; small green diamonds: flux densities at 1365 and 1485 MHz derived from the VLA maps at 20.0″ × 20.0″; large green diamonds: flux densities at 4985 and 8485 MHz, derived from the VLA map at 6.0″ × 6.0″; orange circles: data from the literature. More details on the data are listed in Appendix A. The solid black line represents the best power-law fit to the data. The dotted black lines enclose the range of variation of the best-fit line according to the uncertainties in the best-fit parameters.

Appendix B). In particular, in the northern tail beyond region N5, the 6.0″ × 6.0″ LOFAR map clearly shows emission with a high average signal-to-noise ratio (S/N ≃ 7) out to $\delta \simeq 39^\circ\,33'$; the emission of this source region was only marginally detected in the VLA observations at 1365 MHz with the same angular resolution. On the other hand, at a lower angular resolution (20.0″ × 20.0″), emission out to that distance from the core is detected in both our LOFAR map at 145 MHz (Fig. 2, right panel) and the VLA maps at 1365 MHz and 1485 MHz. However, the LOFAR map reveals an additional detail with respect to the VLA maps: beyond region N5, the radio emitting plasma bends from the north-east direction to the north direction at a declination $\delta \simeq 39^\circ\,32'$. This feature was not clearly seen before, even though hints of a change in the direction of the northern tail emerge in our re-analysed archival VLA map at 1485 MHz. A bending of the radio structure about $\delta \simeq 39^\circ\,32'$ is also suggested by the higher angular resolution LOFAR map (Fig. 2, left panel), despite the low S/N of the emission in this region.

In the southern lobe (region S4), the higher angular resolution (6.0″ × 6.0″) LOFAR map (Fig. 2, left panel) reveals ≈2′ (≈43 kpc) of additional faint emission along the east-west direction with respect to the VLA map at 1365 MHz with the same angular resolution. Overall, region S4 in the LOFAR maps at 145 MHz appears to have an area ≈50% larger than in previous VLA maps at 1365 MHz with the same angular resolution. Furthermore, region S4 displays a protuberance on the eastern side which extends for ≈2′ (≈33 kpc) in the east-west direction, and which was partly detected only in our re-analised VLA map at 1365 MHz and 1485 MHz with resolution of 20.0″ × 20.0″; it was not deteced by the VLA at 6.0″ × 6.0″ resolution.

We highlight that the southern additional, extended emission of 3C 449 recovered by LOFAR at both angular resolutions and by the VLA at 20.0″ × 20.0″ was actually detected in previous observations performed with the Westerbork Synthesis Radio Telescope (WSRT) at 608 MHz[4]. However, the larger beam (48.0″ × 30.0″) of the WSRT map makes this map unsuitable for a comparison with the LOFAR and VLA maps presented in this work.

3.2. Spectral index maps and profiles

3.2.1. Map characteristics

Following the procedure described in Sect. 2.2 to make the spatial resolution of the VLA maps match the resolution of our LOFAR maps, we derived four different maps of the radio spectral index α by combining in pairs the four maps obtained at the frequencies of 145, 1365, 4985, and 8485 MHz. As mentioned in Sect. 2.2, the data were restricted to have the same (u, v) range. Specifically, for the 145−1365 MHz spectral index map, the (u, v) range is $(150, 51\,000)\,\lambda$, for the 1365−4985 MHz spectral index map $(u, v) = (600, 51000)\,\lambda$, and for the 4985−8485 MHz spectral index map $(u, v) = (900, 56\,300)\,\lambda$. Three out of four spectral index maps have an angular resolution of 6.0″ × 6.0″. The remaining map has an angular resolution of 20.0″ × 20.0″. To build these spectral index maps, in each single-frequency map, we selected only pixels whose surface brightness was above $10\sigma_{\rm rms}$ (with $\sigma_{\rm rms}$ as the rms noise level of the map).

Figure 3 shows the spectral index maps at 6.0″ × 6.0″ angular resolution: the top left, middle, and right panels display the spatial distribution of the spectral index, α, in the 145−1365 MHz, 1365−4985 MHz, and 4985−8485 MHz frequency ranges, respectively; the bottom row shows the corresponding maps of the 1σ uncertainty on the spectral index, σ_α. In the panels of the top row, source regions with lower values of the spectral index, i.e. with flatter spectra, are represented in blue, while source regions with steeper spectra are displayed in green-red colour. In the bottom row, bluer (redder) colours represent lower (higher) values of σ_α. Figure 4 shows the spectral index maps at 20.0″ × 20.0″ angular resolution (left panel), with the corresponding map of σ_α (right panel).

We note that the three spectral index maps of Fig. 3 have different spatial extensions: while the map on the left panel has a full extension of ≈15′ (≈324 kpc), the maps in the middle and right panels have a full extension of ≈11′ (≈238 kpc) and ≈7′ (≈151 kpc), respectively. The smaller extension of the latter two spectral index maps is the result of the smaller extension of the source in the VLA maps at 4985 MHz and 8485 MHz (see Sect. 3.1). The spectral index map of Fig. 4 has a full extension of ≈20′ (≈432 kpc).

3.2.2. Radial variations of the spectral index

A visual inspection of the 6.0″ × 6.0″ angular resolution spectral index maps of Fig. 3 shows that, in all of the three frequency ranges, the spectral index α on average stays roughly constant ($\alpha \approx 0.6$) along the straight, inner jet, out to regions N1 and S1; starting from the inner lobes (regions N2 and S2), it then gradually increases with the distance to the radio core out to the source edges, implying that the average source spectrum steepens as the radio-emitting plasma propagates outwards, as expected from particle ageing in absence of significant re-acceleration processes. This behaviour is also apparent in the 20″ × 20″ angular

[4] The WSRT image is available in the online 3CRR Atlas (https://www.jb.man.ac.uk/atlas/), which presents radio images and other data for the nearest 85 DRAGNS (radio galaxies and related objects) in the so-called 3CRR sample of Laing et al. (1983).

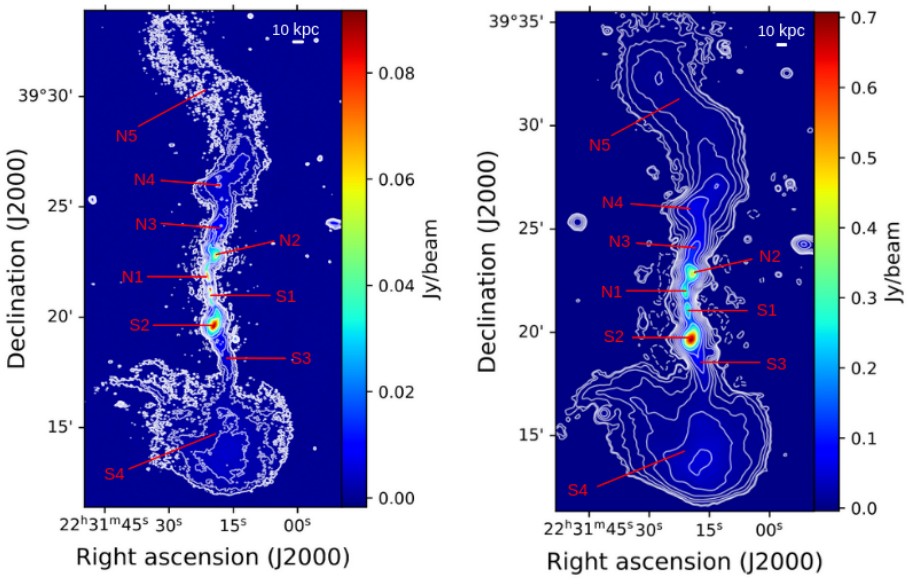

Fig. 2. LOFAR maps of 3C 449 at 145 MHz. Left panel: Angular resolution of 6.0″ × 6.0″. The contour levels are [–0.07%, 0.07%, 0.08%, 1.6%, 3.2%, 6.4%, 12.8%, 25.6%, 51.2%] × the flux peak of 0.09 Jy/beam. The rms noise of the map is 0.1 mJy beam^{-1}. Right panel: Angular resolution of 20.0″ × 20.0″. The contour levels are [–0.015%, 0.015%, 0.02%, 0.04%, 0.08%, 1.6%, 3.2%, 6.4%, 12.8%, 25.6%, 51.2%] × the flux peak of 0.7 Jy beam^{-1}. The rms noise of the map is 0.2 mJy beam^{-1}.

resolution spectral index map at 145-1365 MHz, shown in Fig. 4 (left panel).

The evolution of the average radio spectrum with increasing distance from the radio core can be better appreciated in the spectral index radial profiles shown in Fig. 5, derived from the 6″ × 6″ angular resolution maps of Fig. 3. Here, each spectral index profile shows the average value of the spectral index, α, as a function of the projected distance from the radio core, r in a given frequency range. The average value of α is computed over a source slice arranged along the east-west direction; the slice thickness $\Delta\delta$ (with δ the declination) is of one pixel, namely 1.5″; r increases from the core outwards along the direction of the declination, roughly corresponding to the jet direction.

Incidentally, we note that, at any given r, the average value of the spectral index shown in each of the profiles of Fig. 5 may be higher than the value of the spectral index that appears to be dominant in the maps of Fig. 3. This is the result of averaging the spectral indices over a jet slice that displays a flatter spectrum in its central part, and a significant spectral steepening in its external part (see Sect. 3.2.3 for details).

Each of the radial profiles of Fig. 5 shows that the spectral index value stays roughly constant within ≈40−50″ from the core (i.e. in regions N1 and S1), despite the small-scale fluctuations, and then significantly increases with increasing distance from the core in both jets. This confirms that, in any given frequency range, the spectrum steepens with the distance from the core beyond regions N1 and S1.

The behaviour we observed in 3C 449 confirms previous findings by Katz-Stone & Rudnick (1997) and Feretti et al. (1999) on this source: they showed that the radio spectrum is roughly constant out to ≈1′ from the core on both sides, and then steepens with increasing distance out to ≈2.5′ from the core (the spatial limit of their spectral studies). The steepening of the spectrum with core distance on arcminute scales also confirms earlier results by Jaegers (1987) and Andernach et al. (1992). This spectral behaviour is typical of FRI radio galaxies (see also, e.g. the case of 3C 31; Heesen et al. 2018), where particle acceleration processes are thought to occur closer to the core, and the accelerated particles radiatively age as the radio source propagates outwards.

A comparison of the three maps of Fig. 3 and of the corresponding radial profiles of Fig. 5 shows that, globally, the radial evolution of the spectral index is different in different frequency ranges. More in detail, the radial profiles are consistent with one another, at the 1σ level, within ≈50″ from the core (i.e. within regions N1 and S1): thus, in this region, the average source spectrum is consistent, within the uncertainties, with a single power law (with $\alpha \simeq 0.6$) over the full, 145-8485 MHz frequency range. However, beyond ≈50″, the radial profiles display a positive vertical offset, on arcminute scale, even though fluctuations are observed on smaller scales: the higher-frequency spectral indices are always higher than the lower-frequency indices. This means that the spectral shape deviates from a single power law, and a spectral curvature appears that makes the spectrum steeper at higher frequencies. Furthermore, the increase of the average spectral index with the distance to the radio core appears to be faster at higher frequencies, indicating that the spectral curvature increases, and the break frequency decreases, with the distance to the core.

The spectral evolution with core distance is not symmetric about the core at all scales and in all frequency ranges. The onset of the spectral curvature appears to become significant (at >1σ) at about the same distance ($r \approx 50''$) from the radio core in the two jet directions, as it can be better appreciated in Fig. 6, an enlargement of Fig. 5 corresponding to the region centred on the radio core and extending from N2 to S2. However, at $r \gtrsim 50''$, different spectral behaviours are observed in the two jet directions in different frequency ranges. Specifically, in the 1365–8485 MHz range (red and blue curves), a spectral steepening with core distance is clearly detected both in the northern and in the southern jet. In the 145−1365 MHz range (green curve) the spectrum flattens, with respect to the inner jet region, between $r \approx 50''$ and $r \approx 100''$ in the northern jet, and between $r \approx 50''$ and $r \approx 80''$ in the southern one: this initial flattening determines the onset of a spectral break in the frequency range 145–4985 MHz. At larger radii, as shown in Fig. 5, the 145−1365 MHz spectrum gradually steepens with distance on both sides, although with asymmetric behaviours: on the northern side, the steepening continues out to region N4 ($r \approx 400''$), where $\alpha \simeq 0.7$, while on the southern one the steepening proceeds out to region S3 ($r \approx 300''$), and then the spectral index

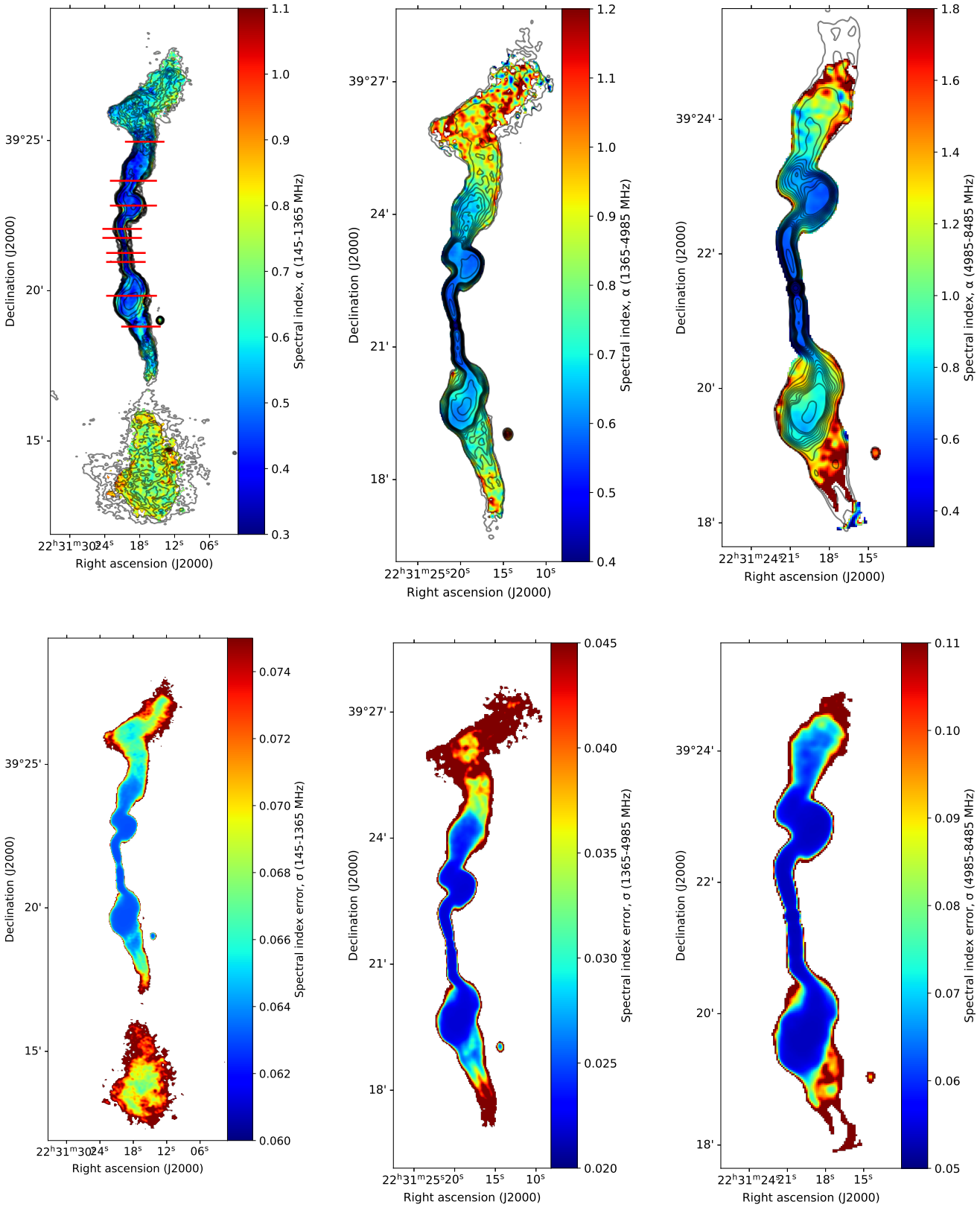

Fig. 3. Spectral index maps at 6.0″ × 6.0″. Top panels: Maps of the radio spectral index of 3C 449 between the frequencies of 145 and 1365 MHz (left), 1365 and 4985 MHz (middle), and 4985 and 8485 MHz (right). Each map is overlaid with surface-brightness contours of the lower frequency map used to compute the spectral index. Bottom panels: Maps of the 1σ uncertainties on the radio spectral index of 3C 449 between the frequencies of 145 and 1365 MHz (left), 1365 and 4985 MHz (middle), and 4985 and 8485 MHz (right). The red segments on top of the map in the top-left panel represent the jet sections selected for the analysis presented in Sect. 3.2.3.

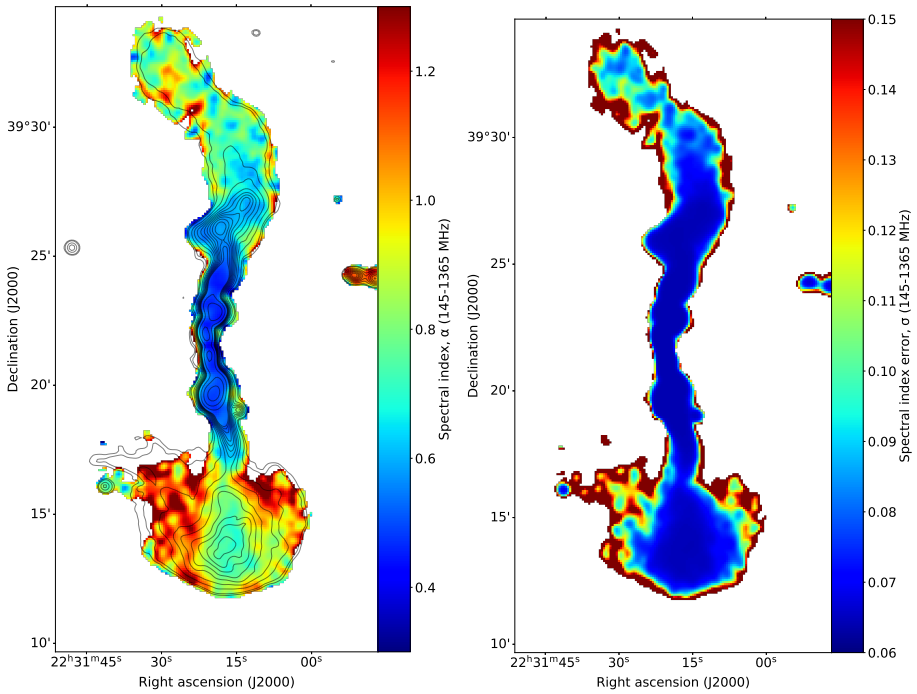

Fig. 4. Radio spectral index of 3C 449 between 145 MHz and 1365 MHz, with the angular resolution of 20.0″×20.0″. Left panel: spectral index map overlaid with 145 MHz surface-brightness contours. Right panel: map of the 1σ uncertainty.

fluctuates about a constant value $\alpha \simeq 0.75$. A flattening of the spectrum beyond region S3 was also observed by Jaegers (1987) at 600–1400 MHz and by Andernach et al. (1992) at 400–2700 MHz.

Overall, in all the frequency ranges considered in this work, a north-south asymmetry in the distribution of α can be appreciated both visually in the spectral index maps and in the radial spectral index profiles on different spatial scales. In particular, in the 4985 − 8485 MHz frequency range, the southern, inner lobe (region S2) appears to have a significantly steeper spectrum than the northern, inner lobe (region N1), as can be seen in the top-right panel of Fig. 3 and in the blue profile in Fig. 6; in the 145−1365 MHz frequency range, the southern, outer lobe (region S4) displays a significantly steeper spectrum than the northern plume (regions N4–N5), as can be seen in the top-left panel of Fig. 3 and in the green profile in Fig. 6.

Besides showing a different average values of the spectral index, the northern tail and southern lobe also show a different spatial distribution of α at both angular resolutions, as can be partly seen in the top-left panel of Fig. 3 and, more clearly, in Fig. 4 (left panel). The northern, narrow tail of the source (regions N4–N5), which exhibits a low 145 MHz surface brightness everywhere, displays a distribution of the 145−1365 MHz spectral index significantly patchy, whose average value is $\alpha \simeq 0.75$ (with $\sigma_\alpha \simeq 0.10$) at 20″ × 20″ resolution. Conversely, the southern lobe of the source (region S4), characterised by a high 145 MHz surface brightness in the inner region that slowly falls off towards the outskirts of the lobe, has a well-defined spectral index distribution: at 20″ × 20″ resolution, we clearly see that the central, brighter region of the lobe has a significantly flatter spectrum ($\alpha \simeq 0.7$–0.9, with $\sigma_\alpha \simeq 0.06$–$0.07$) than the surrounding, fainter regions ($\alpha \simeq 0.9$–1.3, with $\sigma_\alpha \simeq 0.12$), yielding an overall spectrum which is steeper than that of the northern tail. This result confirms previous findings on the north-south spectral asymmetry by Katz-Stone & Rudnick (1997) and Feretti et al. (1999), also suggested by earlier, lower-resolution studies by Jaegers (1987) and Andernach et al. (1992).

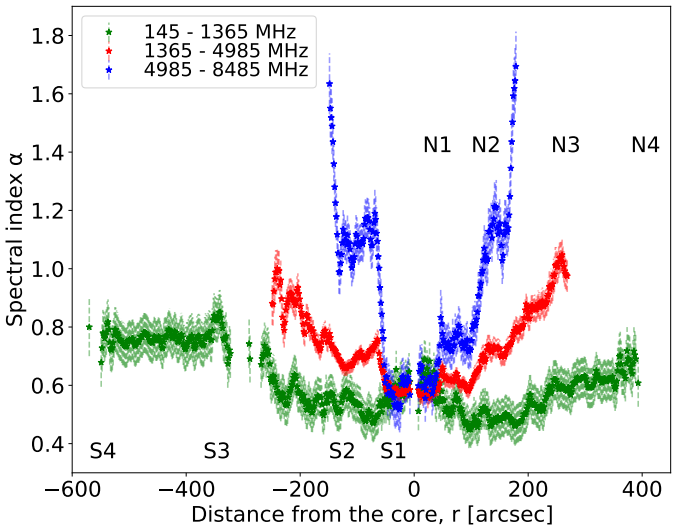

Fig. 5. Radio spectral index, α, in different frequency ranges, as a function of the projected distance from the radio core, r (see text for details), for the northern and southern jets of the source. The position of the core corresponds to $r = 0$; positive distances are for the northern jet, and negative distances for the southern one. The spectral indices of the core are not included in the plot. The frequency ranges and the corresponding colours are listed in the inset. The overall steepening of the spectrum (i.e. an increase of the radio spectral index α) downstream of the jet can be appreciated in all three spectral index profiles.

3.2.3. Transverse variations of the spectral index

Besides showing an evolution of the average spectral index with the distance from the core, our spectral index maps also reveal significant substructures in the distribution of α along the east-west direction. This transverse substructure is clearly detected, in all the explored frequency ranges, from the inner lobes (regions N2 and S2) outwards. However, in the frequency range 145−1365 MHz, a transverse structure in α is also detected

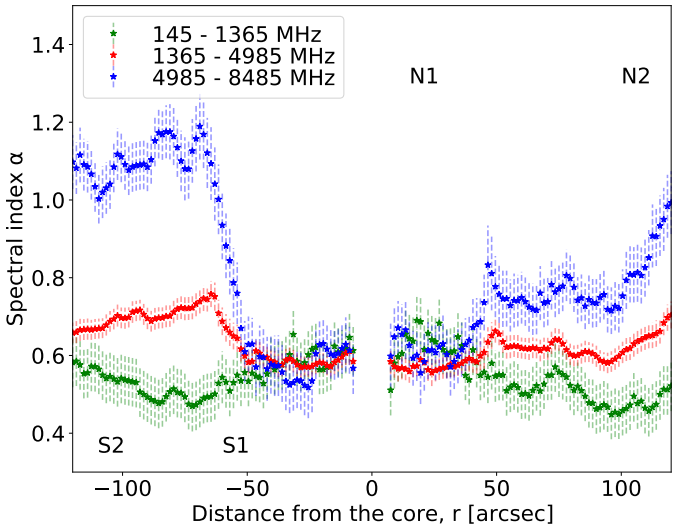

Fig. 6. Same as Fig. 5 but for the inner ≈240″ region of the source.

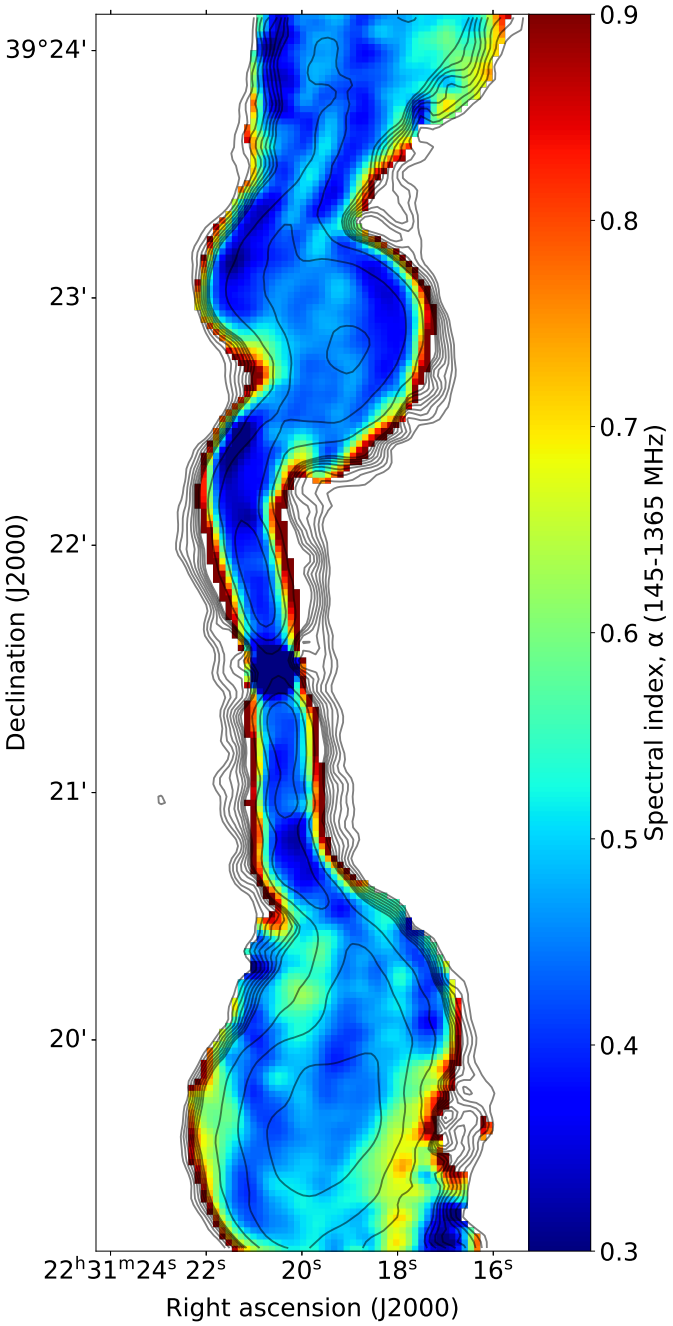

Fig. 7. Enlargement of the inner ≈5′ region of the 145−1365 MHz spectral index map at the angular resolution of 6.0″ × 6.0″ (top-left panel of Fig. 3). The dark-blue patches, representing the flattest spectra ($\alpha \simeq 0.32$–0.35, $\sigma_\alpha = 0.063$), are visible about the jet turns. For the uncertainties, see the bottom-left panel of Fig. 3.

both in the northern and in the southern inner jet, specifically in the nearly straight and collimated structures that extends out to ≈1′ from the radio core (regions N1 and S1) . As shown in the higher angular resolution, 145−1365 MHz spectral index map of Fig. 3 (top-left panel) and in its ≈5′ enlargement of Fig. 7, as well as in the lower angular resolution maps of Fig. 4 (left panel), the higher surface-brightness part of each of the inner jets, closer to the jet axis, is characterised by a flat spectrum (blue colour, $\alpha \simeq 0.4$), and appears to be surrounded by layers whose spectra are significantly steeper (green-red colour, $\alpha \simeq 0.6$–1.1).

In both jets, about the first turn, at a distance of ≈1′ from the core, the spectral index distribution starts to become more complex: the steep spectrum regions seem to be responsible for the widening of the source, and appear to be progressively mixed to a less collimated, although continuous, flat spectrum structure that extends with no interruptions out to ≈3′ from the core (regions N2–N3) for the northern jet, and out to ≈2.5′ from the core (region S2) for the southern jet.

The evidence of a flat spectrum jet spine surrounded by a steeper spectrum sheath in the inner, ≈1′ jets of 3C 449 is a unique feature of our 145−1365 MHz spectral index maps, which combine LOFAR and VLA data. In the remaining explored frequency ranges, from 1365 to 8485 MHz (see middle and right panels of Fig. 3), in the first ≈1′ of the jet we do not clearly detect a flatter spectrum jet surrounded by a steeper spectrum layer. However, beyond ≈1′ from the core, we do see that steeper spectrum regions appear to enshroud a flatter spectrum jet, in both jets and in all of the three spectral index maps of Fig. 3: the steep spectrum regions widen with the distance from the core, and start to become patchy about the edge of the collimated jet, namely in regions N4–N5 for the northern jet, and in region S3 for the southern jet; beyond these regions, there is no clear structure in the distribution of the spectral index in the northern plume, whereas the southern lobe displays a flatter core surrounded by a steeper shell, as mentioned in Sect. 3.2.2.

The presence of a flat-spectrum jet spine surrounded by a steep-spectrum sheath in the inner jet of 3C 449 can be better visualised by the transverse profiles of the spectral index, shown in Fig. 8. These profiles were constructed for a number of representative source slices arranged in the east-west direction on the 145−1365 MHz spectral index map at 6″×6″ angular resolution, covering both the northern and the southern jets. The slices are highlighted with red segments in the top-left panel of Fig. 3.

In Fig. 8, the left panel shows the southern jet and the right panel shows the northern jet. The transverse spectral index profiles of slices selected at different distances from the core are represented with different colours. Out to ≈100″ from the core, in each profile the spectral index is lower (i.e. the spectrum is flatter) about the slice centre (close to the jet axis), where $\alpha \simeq 0.4$–0.6, and becomes larger and larger (i.e. the spectrum steepens) as one moves towards the eastern and western edges of

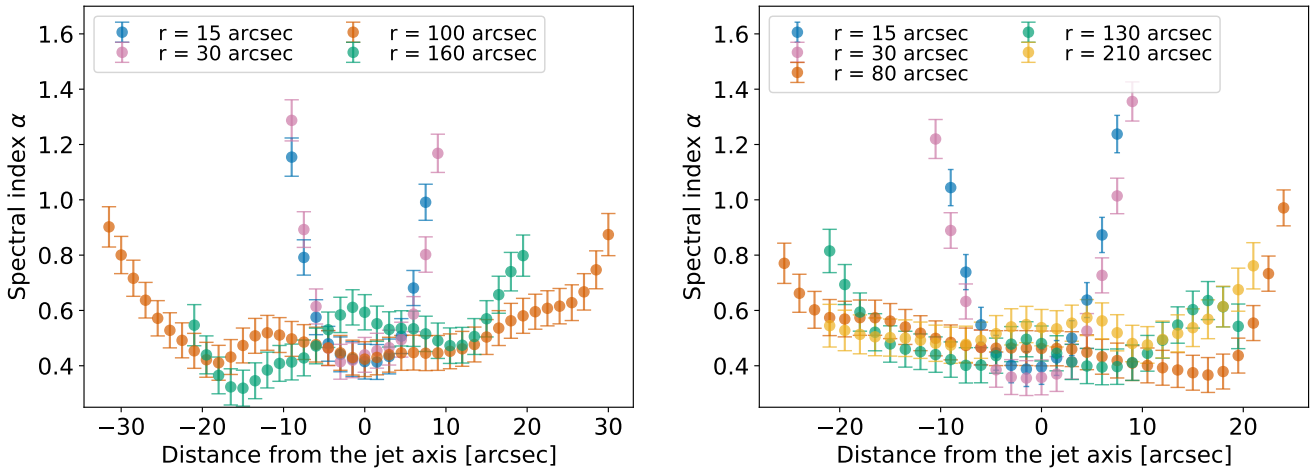

Fig. 8. Transverse profiles of the spectral index between 145 and 1365 MHz, derived from the $6'' \times 6''$ spectral index map: each profile is evaluated over a slice arranged along the east-west direction, perpendicular to the jet axis; the slice thickness is 1 pixel (i.e. 1.5″). All the slices are shown in the top-left panel of Fig. 3. Left panel: southern jet. Right panel: northern jet.

the slice (far from the jet axis), where the spectral index reaches values of $\alpha \simeq 1.3$ in the jet regions closer to the core.

The steeper spectrum sheath is narrower (a few arcseconds across) and displays a faster rise of the spectral index in slices located at smaller distances from the radio core; it widens and displays a more gradual rise of the spectral index as the slice distance from the radio core increases. About $\approx 3'$ from the core in the northern jet, and about $\approx 2.5'$ in the southern jet, the shape of the profiles becomes more complex, and the separation between a flat jet spine and a steep sheath structure is no longer clear. In these regions, the central, flatter-spectrum structure fades, and mixing between the flatter-spectrum and steeper-spectrum regions seems to occur.

The evidence we found of a steep spectrum sheath embedding the flatter spectrum jet beyond $\approx 1'$ from the core confirms previous findings by Katz-Stone & Rudnick (1997) in the 330–4835 MHz frequency range for both jets; it also confirms the results obtained by Feretti et al. (1999) in the 4985–8400 MHz frequency range for the southern jet, but not for the northern jet, where these authors do not identify a spine-sheath structure. On the other hand, our results on the transverse spectral index structure of the inner, $\approx 1'$ jet in the 145−1365 MHz range were not reported previously. We discuss the possible origin of the spine-sheath spectral structure in Sect. 5.2.2.

3.2.4. Substructures with very flat spectrum

A noteworthy aspect of our spectral index maps relates to the unusually low values that the 145−1365 MHz spectral index assumes in some regions of the source. Both the higher angular resolution spectral index maps (top-left panel of Fig. 3, and its enlargement of Fig. 7) and the lower angular resolution map (left panel of Fig. 4) show that, in this frequency range, the spectrum is very flat, with $\alpha \simeq 0.35-0.45$, in significant portions of jet regions N1, N2, N3, S1, and S2. Furthermore, a few isolated substructures display an even flatter spectrum, with $\alpha \simeq 0.30-0.35$; they appear about the eastern jet turns of the northern, inner jet (in regions N1 and N2) and the western turn of the southern, inner jet (in region S1), and have a linear size of $\approx 10''$ (≈ 3.6 kpc). The uncertainty on α is $\sigma_\alpha \simeq 0.06$ across the entire jet region, making all the α values we measured be consistent with the 'universal' spectral index value of 0.5 (expected from diffusive shock acceleration of particles by non-relativistic, strong shocks; see Sect. 5.2.1) at the $2-3\sigma$ level. Some of them have a counterpart in the 1365−4985 MHz and/or the 4985−8485 MHz frequency range. However, at these frequencies, their spectrum always has an index $\alpha > 0.5$, consistent with the spectral index of the adjacent regions at 1σ level; therefore, the spectral flattening of these regions at 1365−4985 MHz has a lower significance than the flattening of the same regions at 145−1365 MHz. Specifically, the 1365−4985 MHz map (Fig. 3, middle panels) shows a counterpart of all of the three flattest substructures detected in the 145−1365 MHz frequency range: the substructures in regions N1 and S1 display $\alpha \simeq 0.54$ (against $\alpha \simeq 0.57$ for the adjacent region), whereas the substructure in region N2 shows $\alpha \simeq 0.57$ (against $\alpha \simeq 0.63$ for the adjacent region). On the other hand, in the 4985−8485 MHz spectral index map, only the flat substructure of region N2 has a counterpart, with $\alpha \simeq 0.57$ (lower than the adjacent region, with $\alpha \simeq 0.65$); no counterpart is detected for the flat substructures in N1 and S1. Interestingly, the flatter-spectrum regions do not display an enhanced surface brightness in any of the observing frequencies (see Fig. 2 and Appendix B.)

We note that the flatter-spectrum regions that we identify were not found in the 2.5″ resolution spectral index maps of the source at 4985–8485 MHz by Feretti et al. (1999), nor in the 3.6″ resolution spectral index map at 1445–4835 MHz by Katz-Stone & Rudnick (1997). No comparison with previous spectral images could be performed at 145–1365 MHz, due to the lack of spectral studies in this frequency range prior to ours.

We discuss the possible origin of the unusually low values of the spectral index detected in the 145−1365 MHz frequency range, as well as of the flattest substructures of regions N1, N2, and S1 in the different frequency ranges in Sect. 5.2.1.

4. Spectral analysis and implications

The spatial distribution of radio spectral indices in radio galaxies is traditionally interpreted as the sign of a radiative ageing of a population of emitting electrons with a power-law energy distribution. In this scenario, a spatial distribution of spectral ages across the source can be inferred either from the spatial distribution of spectral break frequencies by using analytical

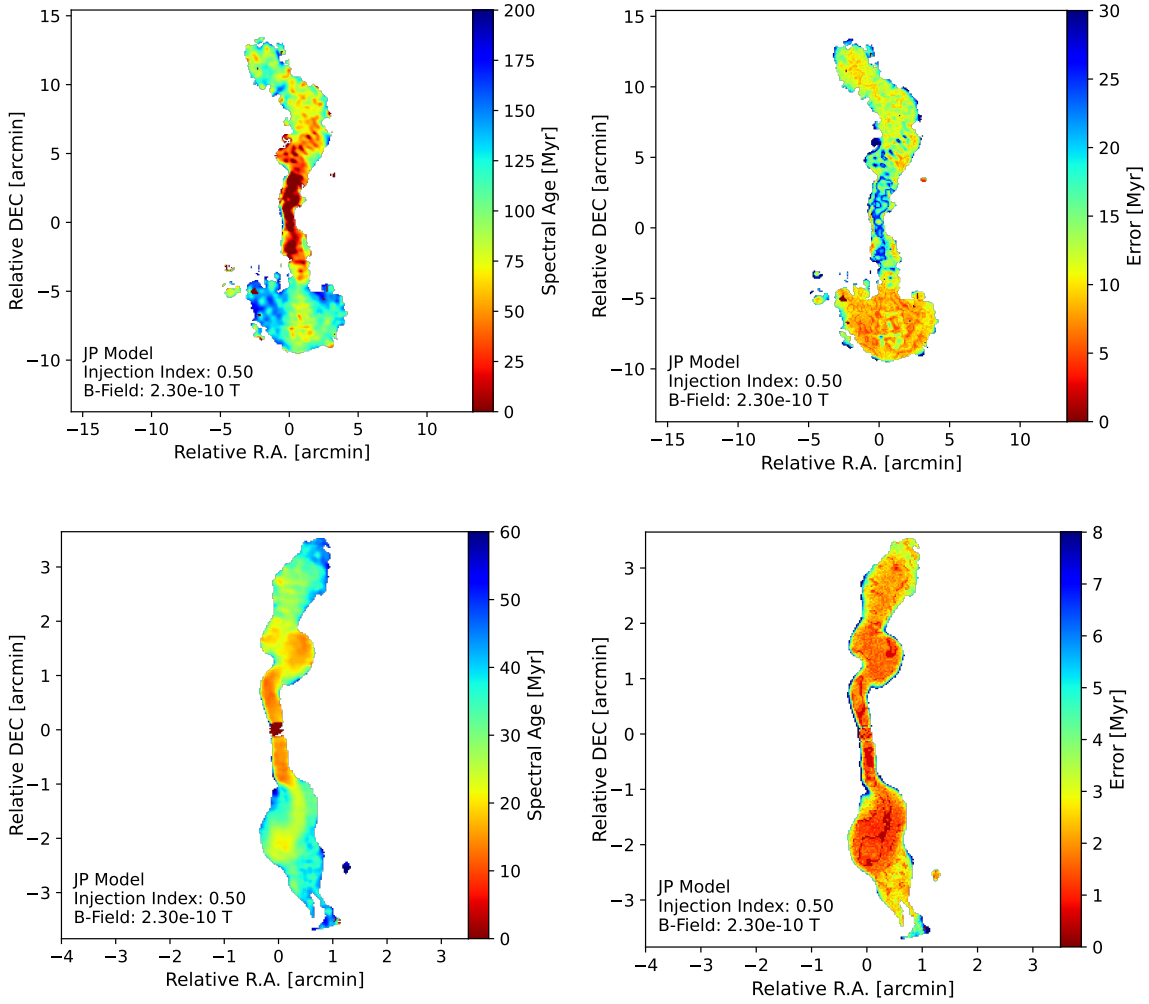

Fig. 9. Spectral ageing maps obtained by fitting the JP model to the intensity maps, and corresponding maps of the uncertainty. Top-left panel: Map of the spectral age of 3C 449 between 145, 1365, and 1485 MHz, with the angular resolution of 20.0″ × 20.0″, by means of the BRATS software package. Top-right panel: Map of the upper error on the spectral age shown in the left panel. Bottom-left panel: Map of the spectral age of 3C 449 between 145, 1365, 4985, and 8485 MHz, with angular resolution of 6.0″ × 6.0″. Bottom-right panel: Map of the upper error on the spectral age shown in the left panel. In all the maps, the assumed magnetic field intensity is $B = B_{\rm eq} = 2.3\,\mu$G.

formulae (e.g. van der Laan & Perola 1969) or from the numerical modelling of the observed radio spectra as the result of the time evolution of an injected spectrum due to plasma radiative losses (Jaffe & Perola 1973; Kardashev 1962; Harwood et al. 2013, 2015). In both approaches, the assumption of a uniform magnetic field in the whole source is common (e.g. Parma et al. 1999; Brienza et al. 2020), even though for a few sources spectral ages and/or break frequencies were estimated in different source points or regions, for which different magnetic field intensities were estimated (e.g. Andernach et al. 1992; Heesen et al. 2018; Kukreti et al. 2022). Alternative scenarios call into question non-uniform magnetic fields with complex structure, electron energy distributions that deviate from a power-law, adiabatic expansion of the jet, or a combination of these effects (Eilek & Arendt 1996; Eilek et al. 1997; Katz-Stone & Rudnick 1997).

Under the traditional ageing assumption, we mapped the spectral age of 3C 449 by carrying out a spectral analysis of our radio maps by means of the Broadband Radio Astronomy ToolS[5] software package. BRATS provides, among other tools, the implementation of a variety of spectral ageing models. Assuming that the radiative losses dominate over the expansion losses, these models compute, for a spatially resolved radio source, the temporal evolution of a power-law synchrotron spectrum as a function of position in the source, accounting for the radiative losses of the plasma due to both synchrotron emission and inverse-Compton scattering of the cosmic microwave background (CMB) off plasma electrons in a magnetic field that does not vary with time. From the spectral shape at each position, the models provide the time since the particles located in that position were last accelerated; from the particle radiative ages, the spectral age of the source can be inferred. Among the models implemented in BRATS, we only considered models that assume a single injection of accelerated particles in the jet at a given epoch. These models are suitable for spatially resolved spectral studies: on small scales, particles can be considered as affected by the same acceleration event.

We considered all the single injection models implemented in BRATS, namely, the Jaffe-Perola's model (Jaffe & Perola 1973), hereafter referred to as the JP model, the Kardashev-Pacholczyk model (Kardashev 1962; Pacholczyk 1970), hereafter referred to as the KP model, and the Tribble model (Tribble 1991, 1993).

[5] https://github.com/JeremyHarwood/BRATS (BRATS; Harwood et al. 2013, 2015).

Both the JP and KP models assume a uniform magnetic field distribution along the source. While in the JP model each electron is subject to multiple scattering events that randomise its pitch angle (i.e. the angle between the electron velocity vector and the magnetic field), in the KP model each electron has a constant pitch angle, implying that more higher-energy electrons can be found at small pitch angles. As a result, the JP model spectrum is steeper than the KP counterpart at high frequencies, due to the ability of high-energy electrons at small pitch angles to radiate at higher frequencies (Katz-Stone & Rudnick 1997; Harwood et al. 2013; Brienza et al. 2020). On the other hand, the Tribble model assumes the magnetic field to be turbulent and describes it as a Gaussian random field; in the weak-field, strong-diffusion case, the magnetic field distribution is drawn from a Maxwell-Boltzmann distribution within each volume element (Tribble 1991; Hardcastle 2013).

We applied the JP, KP, and Tribble models to both higher ($6'' \times 6''$) and lower ($20'' \times 20''$) angular resolution intensity maps; therefore, we obtained two spectral age maps per model. The maps obtained with the JP model are shown in Fig. 9; those obtained with the KP and Tribble models are reported in Appendix C.

In all of these figures, the first map (top-left panel), obtained from the intensity maps at 145, 1365, and 1485 MHz, has an angular resolution of $20'' \times 20''$, and an extension of $\approx 20'$ ($\approx$430 kpc); the second map (bottom-left panel), obtained from the intensity maps at 145, 1365, 4985, and 8485 MHz, has an angular resolution of $6'' \times 6''$ and an extension of $\approx 7'$ ($\approx$150 kpc). The lower resolution, $20'' \times 20''$ spectral age map was obtained from intensity maps at three frequencies only. This restriction may introduce uncertainties in the spectral age due to the sparse sampling of the radio spectrum, but preserves the large scale ($\approx 20'$) of the map. Indeed, including in the analysis our additional intensity maps at 4985 and 8485 MHz, whose field of view is limited to $\approx 10''$ and $\approx 7''$, respectively, would significantly reduce the size of our spectral age map.

The spatially resolved spectral analysis performed with BRATS can be summarised as follows. With an assumed constant magnetic field intensity, BRATS initiates the spectral modelling with a power-law electron energy distribution, $N(E) = N_0 E^{-p_{\rm inj}}$, that generates a synchrotron spectrum $S(\nu) = CE^{-\alpha_{\rm inj}}$, with $\alpha_{\rm inj} = (p_{\rm inj} - 1)/2$ and C a constant of proportionality (Harwood et al. 2013). To carry out the spectral analysis, BRATS divides the source in a number of 'regions'. In each region, the initial spectrum evolves with time, developing a spectral break and a steepening of its higher-frequency portion, according to the spectral ageing model chosen for the analysis. The time, τ, at which the chosen model best fits the spectrum of a given region is selected as the spectral age of that region according to that model. The final result is thus a map of the spectral age of the source for each model considered in the analysis.

To model the spatially resolved spectrum, we employed the JP, KP, and Tribble models assuming an energy injection index $\alpha_{\rm inj} = 0.50$ (i.e. a particle injection index of $p_{\rm inj} = 2.0$). This value of the injection index is the expected lower limit for particles accelerated through the diffusive shock acceleration mechanism in strong, non-relativistic shocks; it is consistent at 3σ level with the flattest spectral index that we measured in the source (see Sect. 3.2.1).

A key ingredient of the JP, KP, and Tribble models is the intensity of the magnetic field, B, in the region of interest. The most recent estimates of the magnetic field of 3C 449 are those made by Hardcastle et al. (1998) and Croston et al. (2003) for the southern lobe of the source. Specifically, these authors found that the equipartition magnetic field evaluated under the assumption that only the relativistic, synchrotron-emitting electrons contribute to the internal lobe pressure, $B_{\rm eq} = 2.3\,\mu$G, renders the lobe under-pressured with respect to the ambient medium. To achieve pressure balance, the authors propose that (i) either magnetic domination holds in the southern lobe, and $B = 12\,\mu$G, or (ii) particle domination holds, and $B = 0.2\,\mu$G. However, from the measured upper limit to the inverse-Compton X-ray flux produced by CMB photons scattered off synchrotron-emitting electrons in the lobe region, the authors derive a lower limit to the magnetic field, $B \geq 0.8\,\mu$G. This limit seems to rule out the above particle-dominated scenario case (with $B = 0.2\,\mu$G), unless the particles contributing to the pressure are non-relativistic electrons, relativistic protons, or entrained and heated thermal material, which do not contribute to the X-ray emission.

Previous estimates of the equipartition magnetic field intensity by Perley et al. (1979) and Andernach et al. (1992) in selected points of the source, by assuming equal energies in relativistic electrons and protons, showed that $B_{\rm eq}$ is not constant across the source, but decreases from the radio core outwards in a similar fashion in the northern and southern source. Specifically, Perley et al. (1979), in their higher-resolution images, found a symmetric decrease of $B_{\rm eq}$ by $\sim$30–40% (from 10.6–11.3 μG to 7–7.3 μG) from the core out to the inner lobes, at $\sim 3'$, highlighting that $B \propto x^{-1}$, with x the cross-sectional radius of the jet; Andernach et al. (1992), from their lower-resolution images, found a fairly symmetric decreasing trend of the magnetic field intensity between $3'$ and $9'$ of the core (where $B_{\rm eq}$ drops from $\simeq$2–2.2 μG down to $\simeq$1–1.2 μG[6]), followed by a further decrease in the northern source, where $B_{\rm eq} \simeq 0.63\,\mu$G at $15'$ north of the core, at the edge of the northern tail. A slight asymmetry emerges on large scales, with the northern tail having a magnetic field intensity a factor $\lesssim$2 lower than the southern lobe. The values of $B_{\rm eq}$ estimated by Perley et al. (1979) and Andernach et al. (1992) at $3'$ differ by a factor of $\gtrsim$3.

For our analysis, we first assumed that equipartition holds for the full source, and adopted the equipartition magnetic field strength estimated for the southern lobe by Croston et al. (2003), $B_{\rm eq} = 2.3\,\mu$G, as the reference value for the isotropic intensity (in the JP and KP models) and for the mean intensity (in the Tribble model) of the magnetic field in each source region.

Even though a careful mapping of the spectral age across the source would certainly require the estimate of $B_{\rm eq}$ at different core distances, adopting the southern lobe's magnetic field value $B_{\rm eq} = 2.3\,\mu$G all over the source enables us to estimate the spectral age of the southern lobe, and to provide an upper limit to the spectral age both in the northern tail, where $B_{\rm eq}$ might be lower than in the southern lobe, and in the jets, where $B_{\rm eq}$ is likely higher than that, according to the trends derived by Perley et al. (1979) and Andernach et al. (1992); we will come back to this aspect at the end of this section. In the following, we describe the results of this analysis.

For comparison purposes, we then repeated the same analysis in a scenario of magnetic domination that guarantees the lobe-ambient pressure balance, by adopting $B = 12\,\mu$G (Croston et al. 2003). These results are reported in Appendix D.

Table 4 shows the results of the fitting procedures with the JP, KP, and Tribble models, with an equipartition magnetic field of $B_{\rm eq} = 2.3\,\mu$G. For each region, BRATS performs a χ^2 test to evaluate the goodness of the spectral modelling and associates

[6] The $B_{\rm eq}$ values from Andernach et al. (1992) are reported here with the appropriate correction to the cosmology adopted in this work.

Table 4. Results of the model fitting for the spatially resolved spectral analysis performed on the intensity maps at 145–1485 MHz, with 20″ × 20″ angular resolution (rows 1–3), and on the intensity maps at 145–8485 MHz, with 6.0″ × 6.0″ angular resolution (rows 4–6).

Frequency range (MHz)	Model	B (μG)	α_{inj}	χ^2_{red}	Confidence bins					Rejected	Median confidence
					<68%	68–90%	90–95%	95–99%	99%		
145−1485	JP	2.3	0.50	3.82	43%	21%	7%	12%	17%	No	<68%
145−1485	KP	2.3	0.50	3.83	43%	21%	7%	12%	17%	No	<68%
145−1485	Tribble	2.3	0.50	3.83	43%	21%	7%	12%	17%	No	<68%
145−8485	JP	2.3	0.50	21.30	38%	27%	10%	14%	11%	No	<68%
145−8485	KP	2.3	0.50	21.42	36%	28%	10%	15%	11%	No	<68%
145−8485	Tribble	2.3	0.50	21.44	36%	28%	10%	15%	11%	No	<68%

Notes. Column 1: Frequency range of the intensity maps used for the spectral analysis; Column 2: Model applied for the spectral analysis; Column 3: Equipartition magnetic field intensity; Column 4: Injection index that best describes the source (i.e. that minimises the mean χ^2_{red} over the source); Column 5: Value of the χ^2_{red} that corresponds to the injection index of Column 4; Columns 6−10: Fraction of adaptive regions that falls in each confidence bin; Column 11: Rejection or non-rejection of the model; Column 12: Median confidence level at which the model cannot be rejected over the entire source.

a confidence level with each region's χ^2 value. The cut-off for the model rejection is set to a confidence level ≥95%. If more than half of the regions fall in the rejection zone, the model over the source is classed as 'poor fit' and is rejected (Harwood et al. 2013). In our case, with one degree of freedom, the median of the confidence levels over the entire source falls in the <68% confidence-level bin for both models: therefore, the two models provide a description of the source spectrum that cannot be rejected at >95% confidence level.

The top panels of Fig. 9 show the results that we obtained by fitting the JP model to the intensity maps at 145, 1365 and 1485 MHz, with an angular resolution of 20″×20″: the left panel displays the map of the spectral age; the right panel shows the corresponding map of the upper error[7]. The spectral age is on average $\tau \lesssim 20$ Myr in the internal part of the jet flow out to ≈3′ from the radio core in the northern jet (i.e. out to region N3), and out to 1′ from the radio core in the southern jet; similar ages appear again in the internal part of region S2, at ≃1.5−2.5′ from the core. The spectral age then increases to $\tau \simeq 30-50$ Myr in the inner flow on larger scales (i.e. in regions N3 and S2–S3). This internal, lower age flow appears to be surrounded by a layer of higher age, $\tau \simeq 70-110$ Myr, which becomes the dominant component beyond those scales.

The northern tail and the southern lobe show a different spectral age distribution, confirming the north-south asymmetry that we detected in the spectral index maps and in the corresponding profiles (see Sect. 3.2). The northern tail shows a spectral age smoothly growing with the core distance, from $\tau \simeq 50$ Myr right beyond region N4 to $\tau \simeq 90-150$ Myr at the edge of the detected emission. In the southern lobe, a central region where $\tau \simeq 70-110$ Myr is surrounded by an older shell whose age is as high as $\tau \simeq 150-200$ Myr.

The bottom panels of Fig. 9 show the results of the spectral age analysis that we performed by fitting the JP model to the 6.0″×6.0″ angular resolution intensity maps at 145, 1365, 4985, and 8485 MHz: the left panel shows the map of the spectral age; the right panel shows the corresponding upper error map. The full extension of this map is smaller (≈7′, from N3 to S3) than that of the map on the top panel, due to the smaller extensions of the 4985 and 8485 MHz surface-brightness maps.

[7] The error on the spectral age is asymmetric, and we report here the upper error, following the suggestion by Harwood et al. (2013).

The obtained age distribution displays a radial dependence and a transverse gradient similar to those of the lower-resolution map, shown in the top panel, on comparable scales. However, differences in the values of the spectral age emerge, owing to the larger set of frequencies used for the analysis and the different angular resolution of the maps. For the northern jet, the internal part of the plasma flow shows ages $\tau \simeq 10-20$ Myr out to ≈2′ from the radio core (i.e. out to region N2); for the southern jet, the internal part shows ages $\tau \simeq 10-20$ Myr out to ≈1′ from the radio core (i.e. out to region S1), and then ages $\tau \simeq 20$ Myr out to ≈2.5′ from the core (i.e. out to region S2). A layer of older particles, with $\tau \simeq 30-50$ Myr, appears to enshroud the younger, internal jets; the older plasma is the dominant component of both jets beyond regions N2 and S2; in the northern jet, region N3 still shows some internal, younger structure, however with a patchy distribution of ages.

In summary, we consider as the spectral age of the northern source side the age of the oldest structure in the northern tail, corresponding to $\tau \simeq 150$ Myr. Similarly, we consider as the spectral age of the southern source side the oldest structure of the southern lobe, corresponding to $\tau \simeq 200$ Myr. The spectral age of the full source can thus be assumed as the higher of the spectral ages of the northern and southern source parts, namely 200 Myr. We note that the spectral ages at the northern edge of the tail (N5) and at the southern edge of the lobe (S4), which are relevant when considering the source expansion (see Sect. 5.1), are both equal to $\tau_{sp} \simeq 150$ Myr. By applying the KP and Tribble model to the same higher and lower angular resolution intensity maps, we obtained results consistent with those obtained with the JP modelling, within the uncertainties. We show the corresponding spectral age maps in Appendix C.

We recall that, for a given break frequency, the spectral age in units of Myr depends on the magnetic field intensity as $\tau \propto B^{1/2}/(B^2 + B^2_{CMB})$ (van der Laan & Perola 1969; Leahy 1991; Parma et al. 1999), where B is the magnetic field strength in the source and $B_{CMB} = 3.18 \times (1+z)^2$ μG is the equivalent magnetic field intensity of the cosmic microwave background radiation, which in turns depend on the redshift z of the source. While we obtained a spectral age $\tau \simeq 150$ Myr with the equipartition magnetic field strength $B_{eq} = 2.3$ μG, the spectral age significantly decreases in the out-of-equipartition scenarios by Croston et al. (2003) mentioned above. Specifically, we obtain $\tau_{sp} \simeq 35$ Myr in a magnetic domination scenario with $B = 12$ μG (see Appendix D), while we estimate $\tau_{sp} \lesssim 124$ Myr for the

inverse-Compton limit $B \geq 0.8\,\mu$G and $\tau_{sp} \simeq 65$ Myr for the particle-dominated scenario with $B = 0.2\,\mu$G. The results we find are expected from the fact that the B/B_{CMB} ratio determines the function $\tau(B)$; for 3C 449, with $B = B_{eq} = 2.3\,\mu$G, the spectral age has its highest possible value at $B \approx B_{eq}$ (see Parma et al. 1999, their Fig. 4). For $B \lesssim B_{eq}$ and $B \gtrsim B_{eq}$, the inferred age is thus lower. This also implies that possible north-south asymmetries in the magnetic field intensities at the source edges, with the northern tail having a magnetic field lower than that of the southern lobe by a factor $\lesssim$2 (as suggested by Andernach et al. 1992), would result in a $\lesssim$20% lower spectral age for the northern tail. The spectral age $\tau_{sp} \simeq 150$ Myr is thus a fairly robust upper limit to the source spectral age. Finally, if the magnetic field intensity had a decreasing trend from the core outwards, reaching the lowest value $B_{eq} = 2.3\,\mu$G in the lobes, the spectral age of the higher-field regions, as the jets and the inner lobes, would be even lower than those we determined by associating the lobe's value with the entire source (see e.g. Appendix D); the increasing trend of the spectral age of the particles from the core outwards would thus be even steeper than observed in our spectral age maps.

The spectral age we estimated for the source assuming $B_{eq} = 2.3\,\mu$G, $\tau_{sp} \simeq 150$ Myr, is higher than the previous estimates of the equipartition spectral age of the source by Andernach et al. (1992) and Parma et al. (1999). Andernach et al. (1992) estimated $\tau \simeq 46\,h^{-3/7}$ Myr and $\tau \simeq 34\,h^{-3/7}$ Myr at distances from the core of 15″ to the north (i.e. beyond the northern edge of the source in our maps) and 9′ to the south, respectively, which correspond to $\tau \simeq 54$ Myr and $\tau \simeq 40$ Myr, respectively, with the value of H_0 we adopted in this work. Parma et al. (1999) estimated a spectral age $\tau \simeq 74$ Myr, which corresponds to $\tau \simeq 87$ Myr with our value of H_0. The discrepancy between their age estimates at equipartition and ours might arise from the fact that both groups made use of equipartition magnetic fields lower than ours (thus much lower than B_{CMB}), and of radio data at higher frequencies and lower angular resolution than ours; furthermore, in Parma et al. (1999), the authors estimated the break frequency by applying the JP model to average radio spectra sampled at two frequencies only.

Our estimate of the spectral age at the source edges is broadly consistent with the estimate of the spectral age of the FRI radio galaxy 3C 31 by Heesen et al. (2018). With a linear size of 1.1 Mpc, 3C 31 is twice as large as 3C 449; these authors estimate its spectral age as $\tau \approx 200$ Myr, ≈25% higher than the age of 3C 449.

5. Discussion

5.1. Spectral age and average expansion speed

The spectral age that we estimated at the edges of the northern tail and the southern lobe in Sect. 4, τ_{sp}, can be used to constrain the time-averaged expansion speed of the radio-emitting plasma through the external medium. This estimate requires the assumption that the above spectral age corresponds to the dynamical age, τ_{dyn}, of the source (i.e. $\tau_{sp} = \tau_{dyn}$). This assumption holds if the particles in the plasma flow were not subject to any in-situ reacceleration or adiabatic loss process during their propagation. In situ re-acceleration would tend to make the electron population younger than it actually is, while adiabatic losses have the opposite effect, because they shift the entire spectrum (and so the break frequencies) to lower frequencies (Katz-Stone & Rudnick 1997).

The dynamical age represents the time that has elapsed since the particle flow was initiated and the radio jet started to propagate through the ambient medium. An estimate of the dynamical age, τ_{dyn}, can be obtained by assuming that each source side has grown to a size D by expanding through the ambient medium with average expansion speed, v_{exp}:

$$\tau_{dyn} = \frac{D}{v_{exp}}. \quad (1)$$

The dynamical age can be re-written as a function of the sound-crossing time, $\tau_{cs} = D/c_s$ (Bîrzan et al. 2008; Wykes et al. 2013), and of the average Mach number, M, as

$$\tau_{dyn} = \frac{D}{M \cdot c_s} = \frac{\tau_{cs}}{M}, \quad (2)$$

where c_s is the sound speed in the X-ray emitting ambient medium, computed as

$$c_s = \sqrt{\frac{\gamma kT}{\mu m_{AMU}}}, \quad (3)$$

with γ the adiabatic index, k the Boltzmann constant, T the temperature of the gaseous medium, μ its mean molecular mass, and m_{AMU} the atomic mass unit. For 3C 449, adopting a mean temperature $T = 1.14 \times 10^7$ K (i.e. $kT = 0.98$ keV), derived by Croston et al. (2003) for the X-ray emitting intergalactic medium of the host galaxy group within a region of radius ≃420″ (≃150 kpc), and assuming $\gamma = 4/3$, the mean sound speed in the medium is $c_s = 458$ km/s. Because of the spatial asymmetry of the source, the sound crossing time is slightly different for the two source sides. Specifically, the estimates of 290 kpc as the distance travelled by the plasma from the core to the edge of the northern tail, and of 200 kpc as the distance travelled by the plasma from the core to the edge of the southern lobe yield sound crossing times $\tau_{cs,N} = 619$ Myr and $\tau_{cs,S} = 426$ Myr for the northern and southern source parts, respectively[8].

In these estimates, the inclination of the source to the plane of the sky, which is <15° according to Feretti et al. (1999), is neglected. If the inclination to the plane of the sky of the lobes of 3C 449 were higher than the inclination of the inner jets, the actual sound-crossing time would be higher. The estimation for the northern jet agrees with the dynamical age of >500 Myr found by Croston et al. (2003) with the same jet length of 290 kpc.

The equivalence of spectral and dynamical age, $\tau_{sp} = \tau_{dyn}$, with the spectral age $\tau_{sp} \sim 150$ Myr derived by assuming equipartition (see Sect. 4), yields the average expansion Mach number of the radio source over its lifetime:

$$M = \frac{\tau_{cs}}{\tau_{sp}}. \quad (4)$$

We obtained $M_N = 4.1$ for the northern part of the source, and $M_S = 2.8$ for the southern part, implying supersonic expansion speeds $v_{exp,N} = 6 \times 10^{-3}\,c$ and $v_{exp,S} = 4 \times 10^{-3}\,c$ towards the north and towards the south, respectively.

[8] We estimated the extension of the northern jet as the sum of the distance of the core to the beginning of region N5, computed along the N-S direction, and the extent of region N5 itself, computed along its symmetry axis, roughly aligned to the NE-SW direction; our estimate agrees with the estimate by Croston et al. (2003). Similarly, we estimated the extension of the southern jet as the distance of the core to the edge of the southern lobe, computed along the N-S direction.

As shown in Sect. 4, in the out-of-equipartition scenarios the spectral ages are always lower than the equipartition spectral age, implying supersonic flows with Mach numbers even higher than those found for the equipartition scenario. Specifically, the magnetic field $B = 12\,\mu$G, that yields $\tau_{sp} \simeq 35$ Myr (see Sect. 4 and Appendix D), implies $M_N \simeq 17.6$ and $M_S \simeq 12.1$; the magnetic field limit $B \geq 0.8\,\mu$G, that yields $\tau_{sp} \lesssim 124$ Myr, implies $M_N \gtrsim 5.0$ and $M_S \gtrsim 3.4$, while $B = 0.2\,\mu$G, that yields $\tau_{sp} \simeq 65$ Myr, implies $M_N \simeq 9.5$ and $M_S \simeq 6.5$.

Observationally, no signature of the strong shocks that are expected for highly supersonic flows was detected in studies of the X-ray emitting gaseous environment of 3C 449 on spatial scales comparable to the full radio source, beyond which the shock is expected to be (Hardcastle et al. 1998; Croston et al. 2003). However, we acknowledge that the sensitivity of ROSAT was not sufficient and that of XMM-Newton (the only instrument currently covering the appropriate spatial scales for 3C 449) may not be sufficient to detect a shock front in the very outer regions of the host galaxy group; therefore, the lack of detection of shock signatures alone does not guarantee that the plasma flow is subsonic. On the other hand, the pressure-balance arguments by Croston et al. (2003, see our Sect. 4) do not support highly overpressured lobes, required for shock generation. Therefore, it is possible that the source is currently expanding with subsonic speed. In this case, $\tau_{dyn} > \tau_{cs}$, and the dynamical age would exceed the spectral age by a factor of $\gtrsim$3–4.

Similar results were obtained for 3C 31: Heesen et al. (2018) infer a time-averaged Mach number $M \approx 5$ from the advection time scale of the oldest visible plasma of the source, assuming no in situ particle acceleration on large scales. However, as claimed by the authors, in 3C 31 a supersonic flow is not in agreement with ram pressure balance arguments, which instead suggest a subsonic flow, at least at the current epoch.

For FRI radio galaxies, subsonic flows on large scales are also suggested by recent 3D MHD numerical simulations: Massaglia et al. (2019, 2022) show that radio galaxies with FRI morphology can be generated by low-power, magnetised jets that propagate in a stratified medium; even though the jet is initially supersonic, a transition to subsonic flow occurs as soon as non-axisymmetric modes develop, which cause the jet disruption and the formation of distorted plumes; the jet head velocity is thus subsonic for a significant fraction of the source lifetime.

In the equipartition scenario, dynamical ages, even when accurately estimated by accounting for the proper density profile of the ambient medium, are actually often found to exceed the spectral ages in large-scale radio galaxies. For instance, in a sample of low-luminosity radio sources of the FRI and FRII type, the correlation between dynamical and spectral ages found by Parma et al. (1999) indicates that the dynamical ages evaluated from ram-pressure arguments are in general larger than the spectral ages derived from a model of aged power-law electron distribution in a uniform magnetic field by a factor $\approx$2–4, depending on the value of the index β in the β-model used to describe the density profile of the external medium. The authors show that the spectral age can increase to become comparable to the dynamical age only when $B_{eq}/B_{CMB} \gtrsim 2$ and $B < B_{eq}$ (see their Fig. 4). However, this is not the case for 3C 449, where $B_{eq}/B_{CMB} \simeq 0.7$, and any deviation from equipartition yields spectral ages lower than the equipartition spectral age, as we illustrated in Sect. 4, preventing the solution of possible discrepancies between dynamical and spectral ages.

In summary, considering a scenario where 3C 449 is expanding with subsonic speed and the magnetic field is constant in time and has either a uniformly distributed intensity across the source (as assumed in Sect. 4) or a gradually decreasing intensity with the distance to the radio core, as suggested by Perley et al. (1979) and Andernach et al. (1992, see also Heesen et al. 2018 for the case of 3C 31), and the spectral age of the source is evaluated from the lobe's magnetic field, a discrepancy between the spectral age and the dynamical age, with $\tau_{dyn} \gtrsim (3-4)\,\tau_{sp}$, emerges. This discrepancy may in principle be solved by assuming that re-acceleration processes take place in the source, naturally lowering the spectral age of the radiating particles. However, evidence of acceleration processes is compelling only in the inner $\lesssim$20 kpc in both jets; therefore, re-acceleration in these regions would probably not significantly impact the spectral age of the particles that have travelled out to the edge of the radio source, at $\approx$200 kpc from the core.

Alternatively, as noted in Sect. 4, the discrepancy between spectral and dynamical age might be solved by interpreting the steepening of the radio spectrum across the source as due to an inhomogeneous magnetic field with more complex structure, rather than to synchrotron ageing (Eilek & Arendt 1996; Eilek et al. 1997; Katz-Stone & Rudnick 1997). In this scenario, the radiating particles might be much older than they look from the break frequency of the radio spectrum, and our spectral ages would no longer be meaningful. However, exploring this scenarios is beyond the scope of this paper.

5.2. Particle populations and acceleration mechanisms

Our LOFAR-VLA spectral index maps, shown in Sect. 3, enabled us to explore the properties of the particle population in 3C 449. On the one hand, as mentioned in Sect. 3.2.2, the radial evolution of the spectral index reveals a particle population that, on scales larger than $\approx$18 kpc, on average progressively loses energy mostly at higher energies as the distance from the radio core increases, without major reacceleration events, as expected for FR I sources (see e.g. the case for 3C 31, Heesen et al. 2018). On the other hand, the small-scale inhomogeneity of the spectral index distribution (see Sect. 3.2.4), and the transverse spectral index profiles, which suggest a spine-sheath structure in the jet (see Sect. 3.2.3), indicate that, even on scales larger than $\approx$18 kpc, energy losses are not exactly as expected in a model where a particle population acquires a power-law energy distribution in an acceleration event, and then radiates in a uniform, constant magnetic field while propagating downstream. Re-acceleration processes may be at work, at least locally, and/or the magnetic field may show complex spatial variation across the jet.

5.2.1. Flat-spectrum substructures

As far as the small-scale inhomogeneities in the spectral index distribution are concerned, as mentioned in Sect. 3.2.4 and shown in Fig. 7, the values of the 145–1365 MHz spectral index are unusually low in significant, coherent portions of jet regions N1, N2, N3, S1, and S2, where $\alpha = 0.35$–0.45, and are even lower in a few, isolated substructures about the eastern jet turns of the northern, inner jet (in N1 and N2) and the western turn of the southern, inner jet (in S1), where $\alpha = 0.30$–0.35. The very low values of α challenge the standard model of diffusive shock acceleration of particles by non-relativistic, strong shocks, which produces spectra with a 'universal' index, $\alpha \geq 0.5$ (Bell 1978); however, the uncertainty on the spectral indices we measure, $\sigma_\alpha \simeq 0.06$, means that the indices are consistent with the theoretical lower limit $\alpha = 0.5$ at the 2–3σ level. Should these

low values of spectral index be confirmed by future observations in the frequency range of a few hundred megahertz (MHz), they might be indicative of acceleration of particles by processes able to generate very flat spectra: for instance, diffusive shock acceleration of particles by strong, relativistic shocks or weak (i.e. barely supersonic) shocks in a hot material can produce spectral indices $\alpha = 0.3-0.5$ (e.g. Peacock 1981); alternatively, very flat spectra may be the result of multiple-shock acceleration mechanisms, able to yield weakly inverted spectra with $\alpha \approx 0$ above the cutoff frequency and $\alpha \approx -0.5$ below the cutoff (e.g. Schneider 1993; Melrose & Crouch 1997). An alternative possibility is that the flattening of the spectrum reflects a local low-frequency spectral turnover in the frequency range of a few hundred MHz, resulting from synchrotron self-absorption. However, current observations are not sufficient for us to make any of these claims.

Regardless of whether the spectral index is larger or lower than 0.5, the coherent, flatter spectrum portions of regions N1, N2, N3, S1, and S2, surrounded by steeper spectrum areas (see Fig. 7) call for a physical interpretation. If the flattening were intrinsic, these regions would be the site of local particle reacceleration; in the spectral ageing maps (see Fig. 9), they clearly appear radiatively younger than their surroundings.

We notice that these flat-spectrum regions are predominantly located in the same positions of the jet bends. As a consequence, as shown in Davelaar et al. (2020), the re-heating of the particles may be due to kink instabilities, which are expected to arise when a jet undergoes changes in its direction of propagation. Alternatively, the presence of these flat-spectrum areas could be attributed to the formation of secondary hotspots, a phenomenon commonly associated with the jet deflection (Scheuer 1982; Hardee & Norman 1990; Cox et al. 1991; Smith 1984; Lonsdale & Barthel 1986; Horton et al. 2023). However, most models predict that these secondary hotspots form as a result of interactions between the jet terminal head and the external medium, and they are typically expected to persist over timescales of several million years (see e.g. Horton et al. 2023). This timescale is inconsistent with the age of tens to hundred million years we estimated for 3C 449 (see Sect. 4). If secondary hotspots formed earlier in the jet's evolution, specifically during its initial expansion into the external medium, they would likely have dissipated by now. Alternatively, Horton et al. (2023) suggest that these secondary hotspots may form as a consequence of the jet stream splitting into two or more parts following the jet interacting with the lobe boundary. The scenario shown in Fig. 5 of their paper for the timestep 131 resembles the situation seen in 3C 449 in region N2. The question is whether such stream splitting happens within an already existing jet. More broadly, the presence of such regions, combined with the apparent change in jet direction, raises the question of whether the jets are undergoing precession, as suggested by Gower & Hutchings (1982, see, however, Lal et al. 2013 for a different interpretation of the wiggles).

A distribution of spectral index similar to that observed in the flat spectrum regions of 3C 449 is reported in the comparable, 144−612 MHz frequency range for the barbell-shaped, giant radio galaxy J223301+131502 (Dabhade et al. 2022). Specifically, in the northern portion of a ∼100 kpc kink structure (see Fig. 6 of their paper), these authors find a spectral index which is as flat as $\alpha = 0.36 \pm 0.08$ in the outer part of the kink and shows a positive gradient across the instability; they interpret the kink as the site of particle acceleration due to a strong shock. This situation strikingly resembles what we see in region N2 of 3C 449.

5.2.2. Spine-sheath spectral structure

As reported in Sect. 3.2.3, and clearly visible in Fig. 7, the LOFAR–VLA spectral index map exhibits a significant transverse gradient in spectral index values. This gradient is very pronounced in the inner ≈10 kpc, where the spectral index increases from $\alpha \simeq 0.4$ in the jet spine to $\alpha \simeq 1.2$ toward the outer sheath, and becomes less pronounced as the distance from the core increases (see Fig. 8). The origin of this steeper spectrum structure remains uncertain. On one hand, we note that our LOFAR-VLA spectral index maps were created by combining data acquired by two different radio telescope arrays, which have significantly different configurations, resulting in distinct (u, v)-coverages that could introduce artificial gradients in the spectral index map. On the other hand, numerical simulations show that a shear layer enshrouding the jet spine can indeed develop in a plasma jet that propagates through a gaseous ambient medium (e.g. Loken et al. 1995; Massaglia et al. 2019): this layer propagates slower than the jet spine (e.g. Massaglia et al. 2019, their Fig. 8), and is composed of a mixture of particles that originates from the interaction of the spine itself with the backflow generated by the interaction of the jet head with the ambient medium. However, the spectral properties of the shear layer are not well-constrained yet. Recent 3D RMHD numerical simulations of jets that account for the evolution of relativistic radiating particles show that relativistic jets can have a spine populated by younger particles, surrounded by a layer populated by older particles (e.g. Mukherjee et al. 2021); however, a direct comparison between simulation and data is still beyond reach. A transverse spectral index gradient similar to the one we observed in 3C 449 was found in other sources as well, including in the inner ≈70 kpc structure of NGC 4869 (Lal 2020), in both jets of 3C 130 (Hardcastle 1999), and in the inner southern jet and in both large scale jets of 3C 465 (Bempong-Manful et al. 2020). Future observations performed at hundreds of MHz will be essential to confirm the presence of a genuine spine-sheath structure.

5.2.3. North-south jet asymmetries

In the northern tail (region N5), the particle spectrum appears to evolve smoothly with increasing distance, gradually steepening as the jet becomes progressively fainter. In contrast, the situation in the southern lobe (region S4) is different. Figure 4 (left panel) illustrates that the spectral index in the central part of the lobe traces the continuation of the jet, which appears to terminate at a distance of 39° 12′, where it likely ceases to propagate into the group intergalactic medium (e.g. Hardcastle et al. 1998). This morphology is likely due to a larger environmental density of the southern lobe compared to the northern tail, as suggested by Hardcastle et al. (1998). The southern jet may not have sufficient momentum to pierce through the denser surrounding medium, and it terminates, giving rise to a backflow. The redirected plasma expands predominantly in the east-west direction, possibly giving rise to the observed steep-spectrum structure that enshrouds the jet termination. Indications of interaction between the radio jet and the X-ray emitting external medium are suggested by Hardcastle et al. (1998) and Croston et al. (2003).

6. Conclusions

In this paper, we investigate the extended emission and spectral properties of 3C 449 by means of new LOFAR observations at 145 MHz, with angular resolution of 20″ × 20″ and 6″ × 6″,

and archival VLA data at 1365, 1485, 4985, and 8485 MHz. Our results can be summarised as follows:

- The high sensitivity and angular resolution of the LOFAR data enabled us to recover the full extent of the previously imaged radio emission of 3C 449 with a resolution of $6.0'' \times 6.0''$ at 145 MHz, unprecedented for this source. The $20.0'' \times 20.0''$ map reveals that the radio-emitting plasma bends from a north-east orientation toward the north at a declination of approximately $\delta \sim 39^\circ\,33'$.
- Combining LOFAR and VLA data, we obtained high resolution spectral index maps of 3C 449 in the 145–8485 MHz frequency range. The 145−1365 MHz spectral index maps show that the source spectrum, on average, stays approximately constant ($\alpha \simeq 0.6$) in the inner, $\approx$40−50″ ($\lesssim$20 kpc) jets (regions N1 and N2), and then progressively steepens with distance from the radio core on both source sides, as expected for an FRI radio galaxy. Small regions with significantly flat spectra ($\alpha \sim 0.30$−0.35, $\sigma = 0.063$) are detected in both jets (regions N1, N2, and S1). In the $20'' \times 20''$ spectral index map, in the northern tail (region N5), we detected a patchy spectral index distribution whose average value is $\alpha \simeq 0.75$; in the southern lobe (region S4) we detected, for the first time, a steep-spectrum region with $\alpha \simeq 0.9$−1.3 surrounding a flatter-spectrum one with $\alpha \simeq 0.7$−0.9.
- Our two spectral index maps at 1365–4985 MHz and 4985–8485 MHz confirm the constancy of the spectral index within $\approx$40−50″ from the core and a progressive spectral steepening beyond that distance.
- The average source spectrum is consistent, within the uncertainties, with a single power law (with $\alpha \simeq 0.6$) over the full, 145–8485 MHz frequency range out to $\approx$50″ from the core (regions N1 and S1). This indicates that particle re-acceleration processes compensate for particle radiative ageing in these regions. Beyond $\approx$50″, a spectral curvature appears that makes the spectrum steeper at higher frequencies, both in the northern and in the southern part of the source. The increase of the spectral index with the distance to the radio core is faster at higher frequencies, implying an increase in the spectral curvature with the distance to the core, in agreement with the expectations for particle synchrotron ageing in absence of significant re-acceleration processes and consistently with the FRI morphology of the source. The localised regions with very flat spectra ($\alpha \simeq 0.30$−0.35), are flatter than the so-called universal spectrum ($\alpha = 0.5$) produced by diffusive shock acceleration by non-relativistic shocks, indicating either the possible presence of re-acceleration processes whose nature cannot currently be established or a spectral turnover due to synchrotron self-absorption. Additional low-frequency observations will be essential to clarify this behaviour.
- The 145−1365 MHz spectral index map reveals, for the first time, a spine-sheath structure in the inner $\approx 1'$ (22 kpc) of both jets: here, a central flat-spectrum spine, with $\alpha \simeq 0.4$, is surrounded by a steeper spectrum layer whose spectral index increases up to $\alpha \lesssim 1.3$, with the highest values reached in the external part of the sheath of the jet regions closer to the core. The spine-sheath structure continues out to $\approx 3'$ (65 kpc) in the northern jet and $\approx 2.5'$ (54 kpc) in the southern jet in the 145−1365 MHz frequency range; beyond $\approx 1'$ from the core, it is also detected in both jets in the higher frequency ranges explored in this paper, confirming previous findings by Katz-Stone & Rudnick (1997) for both jets and by Feretti et al. (1999) for the southern jet. The spine-sheath structure may be the signature of the interaction between jet and ambient medium that emerges in 3D MHD simulations.
- In the standard ageing scenario, we derive the highest radiative age of the emitting particles under the assumption of equipartition and of a constant magnetic field throughout the source. The spectral age maps yields $\tau \lesssim 20$ Myr in the internal jet parts out to $\approx 3'$ from the radio core in the northern jet, and out to $1'$ and about $\simeq$1.5−2.5′ from the radio core in the southern jet. This internal, lower age structure is surrounded by a sheath of higher age, $\tau \simeq 70$−110 Myr, which becomes the dominant component beyond those scales. In the northern tail, the spectral age smoothly grows with the core distance, reaching $\tau \simeq 90$−150 Myr at the edge of the detected emission. In the southern lobe, we detected a central region with $\tau \simeq 70$−110 Myr, which is surrounded by an older region with an age of $\tau \simeq 150$−200 Myr. We estimate $\tau_{\rm sp} \simeq 150$ Myr as the spectral age of the source.
- Assuming that the spectral age of 3C 449 corresponds to its actual dynamical age, we found that the average propagation speed of the source over its lifetime is supersonic: the Mach numbers are $M_{\rm N} \sim 4.1$ for the northern jet and $M_{\rm N} \sim 2.8$ for the southern one when equipartition holds. They are higher in out-of-equipartition scenarios. This finding is against expectations from 3D RMHD simulations of FRI radio galaxies, where the jets stop to be supersonic early in their propagation. If the jets of 3C 449 were indeed subsonic on average, a discrepancy between dynamical and spectral age would appear, with $\tau_{\rm dyn} \gtrsim (3$−$4)\tau_{\rm sp}$. Particle re-acceleration processes occurring in the jets may in principle lower the spectral age of the source; however, evidence of the re-acceleration processes is compelling only in the inner $\lesssim$20 kpc of both jets, and not on larger scales, as required to solve the age discrepancy.

In conclusion, the new LOFAR maps at 145 MHz have significantly enhanced our understanding of the spectral index distribution in 3C 449, while also raising new questions on the nature of the source substructures observed in the 1365−8485 MHz range. Addressing these questions will require additional observations at a few hundred MHz.

Acknowledgements. L.R. is funded by the Deutsche Forschungsgemeinschaft (DFG, German Research Foundation) – project number 443220636. L.R. and L.O. acknowledge partial support from the Italian Ministry of Education, University and Research (MIUR) under the Departments of Excellence grant L.232/2016. The work of L.R. was part of his Master Thesis project at the University of Torino, Italy, in collaboration with the Kapteyn Astronomical Institute, Groningen, The Netherlands. L.O. acknowledges partial support from the INFN Grant InDark. M.J.H. acknowledges support from the UK Science and Technology Facilities Council [ST/ST/Y001249/1]. J.H.C. acknowledges support from the UK Science and Technology Facilities Council (ST/X001164/1, ST/J001600/1). LOFAR is the Low Frequency Array, designed and constructed by ASTRON. It has observing, data processing, and data storage facilities in several countries, which are owned by various parties (each with their own funding sources), and which are collectively operated by the ILT foundation under a joint scientific policy. The ILT resources have benefited from the following recent major funding sources: CNRS-INSU, Observatoire de Paris and Université d'Orléans, France; BMBF, MIWF-NRW, MPG, Germany; Science Foundation Ireland (SFI), Department of Business, Enterprise and Innovation (DBEI), Ireland; NWO, The Netherlands; The Science and Technology Facilities Council, UK; Ministry of Science and Higher Education, Poland; The Istituto Nazionale di Astrofisica (INAF), Italy. This research made use of the Dutch national e-infrastructure with support of the SURF Cooperative (e-infra 180169) and the LOFAR e-infra group. The Jülich LOFAR Long Term Archive and the German LOFAR network are both coordinated and operated by the Jülich Supercomputing Centre (JSC), and computing resources on the supercomputer JUWELS at JSC were provided by the Gauss Centre for Supercomputing e.V. (grant CHTB00) through the John von Neumann Institute for Computing (NIC). This research made use of the University of Hertfordshire high-performance

computing facility and the LOFAR-UK computing facility located at the University of Hertfordshire (https://uhhpc.herts.ac.uk) and supported by STFC [ST/P000096/1], and of the Italian LOFAR IT computing infrastructure supported and operated by INAF, and by the Physics Department of Turin University (under an agreement with Consorzio Interuniversitario per la Fisica Spaziale) at the C3S Supercomputing Centre, Italy. This work made use of Astropy (http://www.astropy.org): a community-developed core Python package and an ecosystem of tools and resources for astronomy (Astropy Collaboration 2013, 2018, 2022). This research has made use of NASA's Astrophysics Data System Bibliographic Services.

References

Andernach, H., Feretti, L., Giovannini, G., et al. 1992, A&AS, 93, 331
Astropy Collaboration (Robitaille, T. P., et al.) 2013, A&A, 558, A33
Astropy Collaboration (Price-Whelan, A. M., et al.) 2018, AJ, 156, 123
Astropy Collaboration (Price-Whelan, A. M., et al.) 2022, ApJ, 935, 167
Becker, R. H., White, R. L., & Edwards, A. L. 1991, ApJS, 75, 1
Bell, A. R. 1978, MNRAS, 182, 147
Bempong-Manful, E., Hardcastle, M. J., Birkinshaw, M., et al. 2020, MNRAS, 496, 676
Best, P. N., & Heckman, T. M. 2012, MNRAS, 421, 1569
Bicknell, G. V. 1984, ApJ, 286, 68
Bicknell, G. V. 1986, ApJ, 305, 109
Bicknell, G. V. 1995, ApJS, 101, 29
Bîrzan, L., McNamara, B. R., Nulsen, P. E. J., et al. 2008, ApJ, 686, 859
Blandford, R., & Eichler, D. 1987, Phys. Rep., 154, 1
Blandford, R. D., & Ostriker, J. P. 1978, ApJ, 221, L29
Brienza, M., Morganti, R., Harwood, J., et al. 2020, A&A, 638, A29
Capetti, A., Macchetto, F., Sparks, W. B., & Miley, G. K. 1994, A&A, 289, 61
Clews, L., Croston, J. H., Dickinson, H., et al. 2025, MNRAS, 541, 3452
Cox, C. I., Gull, S. F., & Scheuer, P. A. G. 1991, MNRAS, 252, 558
Croston, J. H., Hardcastle, M. J., Birkinshaw, M., & Worrall, D. M. 2003, MNRAS, 346, 1041
Croston, J. H., Ineson, J., & Hardcastle, M. J. 2018, MNRAS, 476, 1614
Croston, J. H., Hardcastle, M. J., Mingo, B., et al. 2019, A&A, 622, A10
Czerny, B., & You, B. 2016, Astron. Nachr., 337, 73
Dabhade, P., Shimwell, T. W., Bagchi, J., et al. 2022, A&A, 668, A64
Davelaar, J., Philippov, A. A., Bromberg, O., & Singh, C. B. 2020, ApJ, 896, L31
de Gasperin, F., Dijkema, T. J., Drabent, A., et al. 2019, A&A, 622, A5
de Vaucouleurs, G., de Vaucouleurs, A., Corwin, H. G., Jr., et al. 1991, Third Reference Catalogue of Bright Galaxies (Springer)
De Young, D. S. 1993, ApJ, 405, L13
Drury, L. O. 1983, Rep. Progr. Phys., 46, 973
Eilek, J. A., & Arendt, P. N. 1996, ApJ, 457, 150
Eilek, J. A., Melrose, D. B., & Walker, M. A. 1997, ApJ, 483, 282
Fanaroff, B. L., & Riley, J. M. 1974, MNRAS, 167, 31P
Feretti, L., Perley, R., Giovannini, G., & Andernach, H. 1999, A&A, 341, 29
Fromm, C. M., Perucho, M., Mimica, P., & Ros, E. 2016, A&A, 588, A101
Gendre, M. A., Best, P. N., Wall, J. V., & Ker, L. M. 2013, MNRAS, 430, 3086
Gower, A. C., & Hutchings, J. B. 1982, ApJ, 258, L63
Hardcastle, M. J. 1999, A&A, 349, 381
Hardcastle, M. J. 2013, MNRAS, 433, 3364
Hardcastle, M. 2018, Nat. Astron., 2, 273
Hardcastle, M. J., & Croston, J. H. 2020, New Astron. Rev., 88, 101539
Hardcastle, M. J., Worrall, D. M., & Birkinshaw, M. 1998, MNRAS, 296, 1098
Hardcastle, M. J., Evans, D. A., & Croston, J. H. 2007, MNRAS, 376, 1849
Hardcastle, M. J., Gürkan, G., van Weeren, R. J., et al. 2016, MNRAS, 462, 1910
Hardee, P. E., & Norman, M. L. 1990, ApJ, 365, 134
Hardee, P. E., Cooper, M. A., & Clarke, D. A. 1994, ApJ, 424, 126
Harwood, J. J., Hardcastle, M. J., Croston, J. H., & Goodger, J. L. 2013, MNRAS, 435, 3353
Harwood, J. J., Hardcastle, M. J., & Croston, J. H. 2015, MNRAS, 454, 3403
Heald, G., McKean, J., Pizzo, R., et al. 2010, arXiv e-prints [arXiv:1008.4693]
Heesen, V., Croston, J. H., Morganti, R., et al. 2018, MNRAS, 474, 5049
Horton, M. A., Krause, M. G. H., & Hardcastle, M. J. 2023, MNRAS, 521, 2593
Ineson, J., Croston, J. H., Hardcastle, M. J., et al. 2015, MNRAS, 453, 2682
Jaegers, W. J. 1987, A&AS, 71, 75
Jaffe, W. J., & Perola, G. C. 1973, A&A, 26, 423
Kardashev, N. S. 1962, Sov. Astron., 6, 317
Katz-Stone, D. M., & Rudnick, L. 1997, ApJ, 488, 146
Komissarov, S. S. 1994, MNRAS, 269, 394
Kuehr, H., Witzel, A., Pauliny-Toth, I. I. K., & Nauber, U. 1981, A&AS, 45, 367
Kukreti, P., Morganti, R., Shimwell, T. W., et al. 2022, A&A, 658, A6
Laing, R. A., & Bridle, A. H. 2002a, MNRAS, 336, 1161
Laing, R. A., & Bridle, A. H. 2002b, MNRAS, 336, 328
Laing, R. A., & Bridle, A. H. 2013, MNRAS, 432, 1114
Laing, R. A., & Bridle, A. H. 2014, MNRAS, 437, 3405
Laing, R. A., & Peacock, J. A. 1980, MNRAS, 190, 903
Laing, R. A., Riley, J. M., & Longair, M. S. 1983, MNRAS, 204, 151
Lal, D. V. 2020, AJ, 160, 161
Lal, D. V., Kraft, R. P., Randall, S. W., et al. 2013, ApJ, 764, 83
Leahy, J. P. 1991, in Beams and Jets in Astrophysics, ed. P. A. Hughes, 19, 100
Ledlow, M. J., & Owen, F. N. 1996, AJ, 112, 9
Loken, C., Roettiger, K., Burns, J. O., & Norman, M. 1995, ApJ, 445, 80
Lonsdale, C. J., & Barthel, P. D. 1986, AJ, 92, 12
Lupton, R. H., & Gott, J. R., I. 1982, ApJ, 255, 408
Martel, A. R., Baum, S. A., Sparks, W. B., et al. 1999, ApJS, 122, 81
Massaglia, S., Bodo, G., Rossi, P., Capetti, S., & Mignone, A. 2019, A&A, 621, A132
Massaglia, S., Bodo, G., Rossi, P., Capetti, A., & Mignone, A. 2022, A&A, 659, A139
Matsumoto, J., & Masada, Y. 2013, ApJ, 772, L1
Meliani, Z., & Keppens, R. 2007, A&A, 475, 785
Meliani, Z., & Keppens, R. 2009, ApJ, 705, 1594
Melrose, D., & Crouch, A. 1997, PASA, 14, 251
Millas, D., Keppens, R., & Meliani, Z. 2017, MNRAS, 470, 592
Mingo, B., Hardcastle, M. J., Croston, J. H., et al. 2014, MNRAS, 440, 269
Mingo, B., Croston, J. H., Hardcastle, M. J., et al. 2019, MNRAS, 488, 2701
Mukherjee, D., Bodo, G., Rossi, P., Mignone, A., & Vaidya, B. 2021, MNRAS, 505, 2267
Mullin, L. M., Hardcastle, M. J., & Riley, J. M. 2006, MNRAS, 372, 113
Murgia, M., Fanti, C., Fanti, R., et al. 1999, A&A, 345, 769
Offringa, A. R., van de Gronde, J. J., & Roerdink, J. B. T. M. 2012, A&A, 539, A95
Owen, F. N., & Ledlow, M. J. 1994, ASP Conf. Ser., 54, 319
Pacholczyk, A. G. 1970, Radio Astrophysics. Nonthermal Processes in Galactic and Extragalactic Sources (San Francisco: Freeman)
Parma, P., Murgia, M., Morganti, R., et al. 1999, A&A, 344, 7
Peacock, J. A. 1981, MNRAS, 196, 135
Pearson, T. J., & Readhead, A. C. S. 1988, ApJ, 328, 114
Perley, R. A., & Butler, B. J. 2013, ApJS, 204, 19
Perley, R. A., Willis, A. G., & Scott, J. S. 1979, Nature, 281, 437
Perucho, M. 2020, MNRAS, 494, L22
Perucho, M., & Martí, J. M. 2007, MNRAS, 382, 526
Perucho, M., Martí, J. M., & Hanasz, M. 2005, A&A, 443, 863
Planck Collaboration XIII. 2016, A&A, 594, A13
Prestage, R. M., & Peacock, J. A. 1988, MNRAS, 230, 131
Rieger, F. M., & Duffy, P. 2007, Highlights Astron., 14, 103
Rieger, F. M., Bosch-Ramon, V., & Duffy, P. 2007, Ap&SS, 309, 119
Rosen, A., & Hardee, P. E. 2000, ApJ, 542, 750
Rossi, P., Bodo, G., Massaglia, S., & Capetti, A. 2020, A&A, 642, A69
Rossi, P., Bodo, G., Massaglia, S., & Capetti, A. 2024, A&A, 685, A4
Scaife, A. M. M., & Heald, G. H. 2012, MNRAS, 423, L30
Scheuer, P. A. G. 1982, in Extragalactic Radio Sources, eds. D. S. Heeschen, & C. M. Wade, 97, 163
Schneider, P. 1993, A&A, 278, 315
Shimwell, T. W., Röttgering, H. J. A., Best, P. N., et al. 2017, A&A, 598, A104
Shimwell, T. W., Tasse, C., Hardcastle, M. J., et al. 2019, A&A, 622, A1
Shimwell, T. W., Hardcastle, M. J., Tasse, C., et al. 2022, A&A, 659, A1
Shimwell, T., Hardcastle, M. J., Tasse, C., et al. 2026, A&A, 707, A198
Simon, A. J. B. 1978, MNRAS, 184, 537
Sironi, L., Rowan, M. E., & Narayan, R. 2021, ApJ, 907, L44
Smith, M. D. 1984, MNRAS, 211, 767
Sun, M., Voit, G. M., Donahue, M., et al. 2009, ApJ, 693, 1142
Tadhunter, C. 2016, A&ARv, 24, 10
Tasse, C., Shimwell, T., Hardcastle, M. J., et al. 2021, A&A, 648, A1
Tchekhovskoy, A., & Bromberg, O. 2016, MNRAS, 461, L46
Tribble, P. C. 1991, MNRAS, 253, 147
Tribble, P. C. 1993, MNRAS, 263, 31
Turner, R. J., Rogers, J. G., Shabala, S. S., & Krause, M. G. H. 2018, MNRAS, 473, 4179
Vaidya, B., Mignone, A., Bodo, G., Rossi, P., & Massaglia, S. 2018, ApJ, 865, 144
van der Laan, H., & Perola, G. C. 1969, A&A, 3, 468
van Haarlem, M. P., Wise, M. W., Gunst, A. W., et al. 2013, A&A, 556, A2
van Weeren, R. J., Williams, W. L., Hardcastle, M. J., et al. 2016, ApJS, 223, 2
Wang, Y., Kaiser, C. R., Laing, R., et al. 2009, MNRAS, 397, 1113
Williams, W. L., van Weeren, R. J., Röttgering, H. J. A., et al. 2016, MNRAS, 460, 2385
Wykes, S., Croston, J. H., Hardcastle, M. J., et al. 2013, A&A, 558, A19
Wyndham, J. D. 1966, ApJ, 144, 459
Zirbel, E. L. 1997, ApJ, 476, 489

Appendix A: 3C 449 flux densities

We report in Table A.1 the total flux densities displayed in the spectrum of Fig. 1.

Table A.1. Integrated flux densities of 3C 449 at different frequencies.

Frequency (MHz)	Flux density (Jy)	Reference
86	29.90 ± 1.10	Laing & Peacock (1980)
145	14.56 ± 2.04	this work (LOFAR; 6.0″ × 6.0″)
145	15.10 ± 2.11	this work (LOFAR; 20.0″ × 20.0″)
178	16.20 ± 1.30	Kuehr et al. (1981)
178	11.07 ± 0.6	Kuehr et al. (1981)
178	12.54 ± 0.63	Laing & Peacock (1980)
408	8.08 ± 0.53	Andernach et al. (1992)
408	5.11 ± 0.44	Kuehr et al. (1981)
750	5.35 ± 0.15	Laing & Peacock (1980)
750	5.67 ± 0.16	Kuehr et al. (1981)
750	5.4 ± 0.3	Kuehr et al. (1981)
1365	3.63 ± 0.07	this work (VLA; 20.0″ × 20.0″)
1400	3.8 ± 0.2	Kuehr et al. (1981)
1400	3.4 ± 0.10	Kuehr et al. (1981)
1400	3.67 ± 0.12	Laing & Peacock (1980)
1410	3.69 ± 0.10	Andernach et al. (1992)
1485	3.42 ± 0.07	this work (VLA; 20.0″ × 20.0″)
2695	2.18 ± 0.11	Andernach et al. (1992)
2695	2.5 ± 0.05	Kuehr et al. (1981)
2695	2.48 ± 0.05	Laing & Peacock (1980)
4750	1.33 ± 0.05	Andernach et al. (1992)
4850	1.15 ± 0.17	Becker et al. (1991)
4985	1.18 ± 0.03	this work (VLA; 6.0″ × 6.0″)
5000	1.38 ± 0.14	Kuehr et al. (1981)
5000	1.38 ± 0.07	Laing & Peacock (1980)
8485	0.72 ± 0.02	this work (VLA; 6.0″ × 6.0″)

Appendix B: VLA archival maps

We show in Fig. B.1 the VLA archival maps at 1365, 1485, 4985, and 8485 MHz that were re-analysed in this work.

Appendix C: Spectral ageing maps with the KP and Tribble models

We show the spectral ageing maps that we obtained by fitting the KP (Fig. C.1) and Tribble (Fig. C.2) models, as implemented in BRATS, to the intensity maps of 3C 449. The left panel shows the 145-1485 MHz spectral age map at the angular resolution of 20.0″ × 20.0″; the right panel shows the 145-8485 MHz spectral age map at the angular resolution of 6.0″ × 6.0″. The spectral evolution inferred with both the KP and Tribble model is comparable to that inferred from the JP model within 1σ (see Sect. 4, Fig. 9).

Appendix D: Spectral ageing maps in a scenario of magnetic dominance

We show in Fig. D.1 the spectral ageing maps of 3C 449 obtained by fitting the JP model, as implemented in BRATS, to the intensity maps of 3C 449, by assuming magnetic dominance for the source, with $B = 12\,\mu$G (Croston et al. 2003).

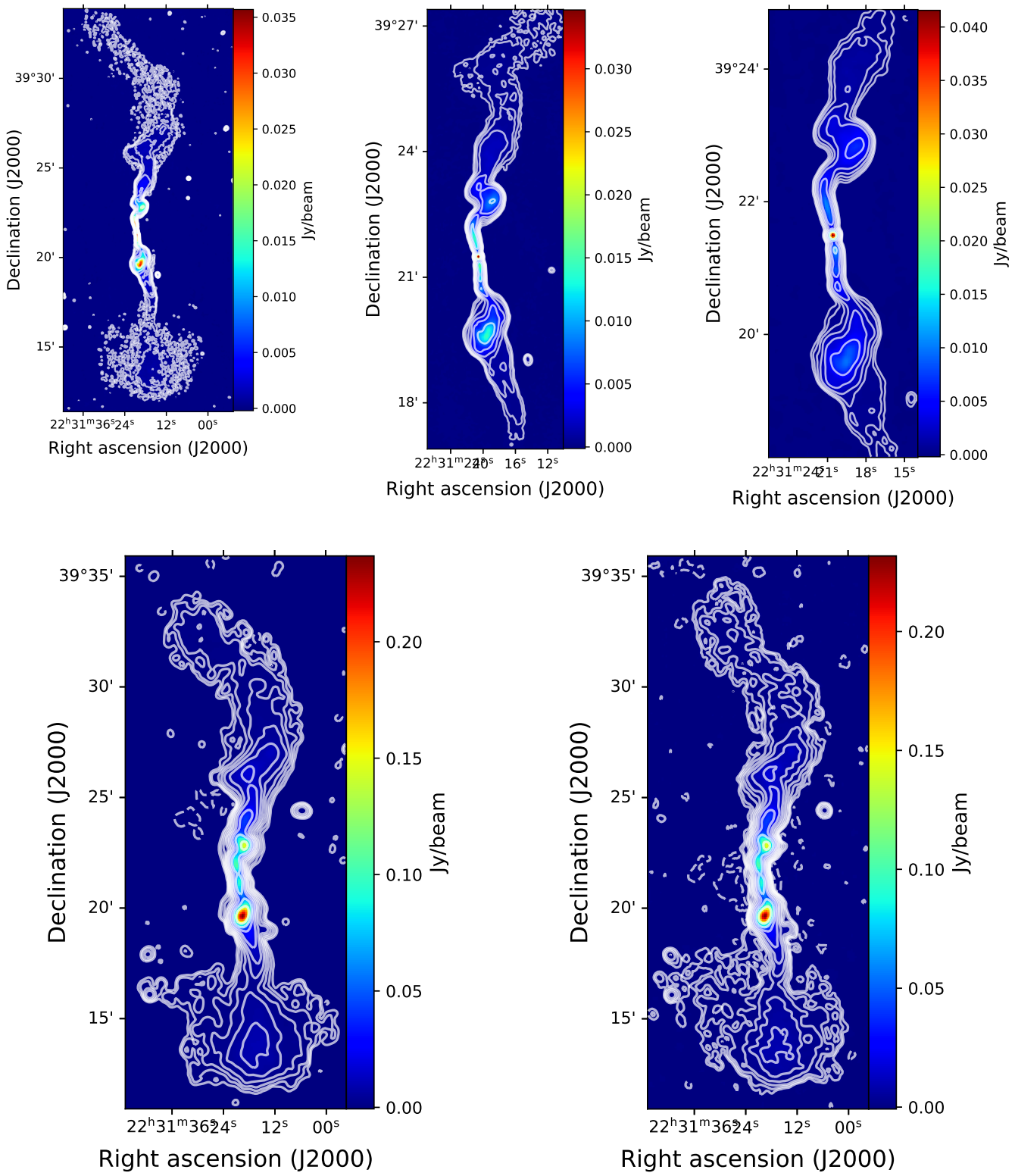

Fig. B.1. VLA maps re-analysed in this work. Top panels: Maps with an angular resolution of 6.0″ × 6.0″. From left to right: i) 1365 MHz VLA map with contour levels [-0.4%, 0.4%, 0.8%, 1.6%, 3.2%, 6.4%, 12.8%, 25.6%, 51,2%] × the peak of 0.035 Jy/beam; ii) 4985 MHz VLA map with contour levels [-0.4%, 0.4%, 0.8%, 1.6%, 3.2%, 6.4%, 12.8%, 25.6%, 51,2%] × the peak of the 0.034 Jy/beam; iii) 8485 MHz VLA map with contour levels [-0.4%, 0.4%, 0.8%, 1.6%, 3.2%, 6.4%, 12.8%, 25.6%, 51,2%] × the peak of 0.041 Jy/beam. Bottom panels: Maps with an angular resolution of 20.0″ × 20.0″. From left to right: i) 1365 MHz VLA map with contour levels [-0.1%, 0.1%, 0.2%, 0.4%, 0.8%, 1.6%, 3.2%, 6.4%, 12.8%, 25.6%, 51,2%] × the peak of 0.239 Jy/beam; ii) 1485 MHz VLA map with contour levels [-0.1%, 0.1%, 0.2%, 0.4%, 0.8%, 1.6%, 3.2%, 6.4%, 12.8%, 25.6%, 51.2%] × the peak of 0.23 Jy/beam.

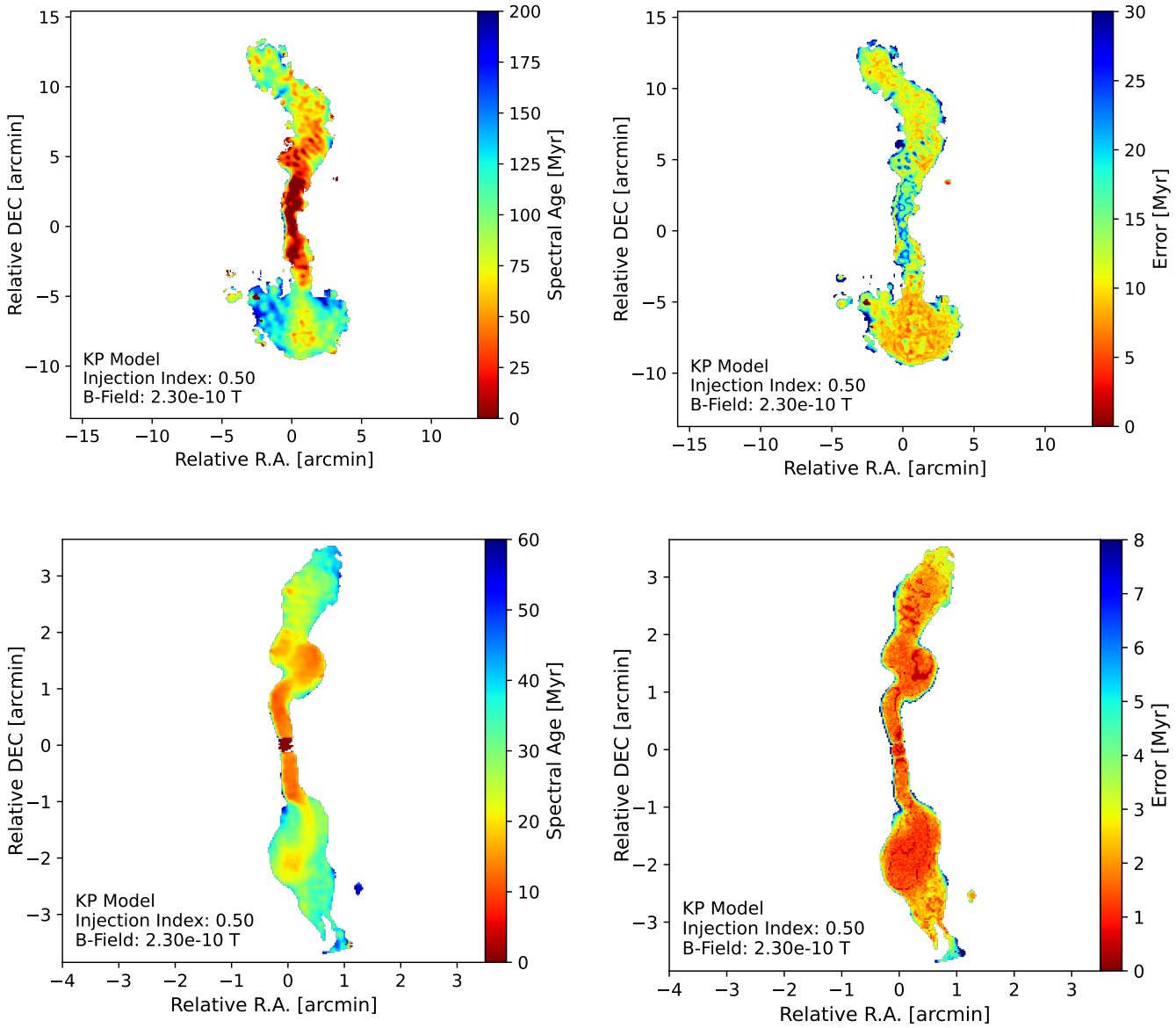

Fig. C.1. Spectral ageing maps obtained by fitting the KP model to the intensity maps, and corresponding maps of the uncertainty. Top-left panel: Map of the spectral age of 3C 449 between 145, 1365, and 1485 MHz, with the angular resolution of $20.0'' \times 20.0''$, by means of the BRATS software package. The parameters of the model are reported in the legend. Overall, the spectral age increases with the distance to the radio core. Top-right panel: Map of the upper error on the spectral age shown in the left panel. Bottom-left panel: Map of the spectral age of 3C 449 between 145, 1365, 4985, and 8485 MHz, with angular resolution of $6.0'' \times 6.0''$. Bottom-right panel: Map of the upper error on the spectral age shown in the left panel. In all the maps, the magnetic field intensity is $B = B_{\rm eq} = 2.3\,\mu$G.

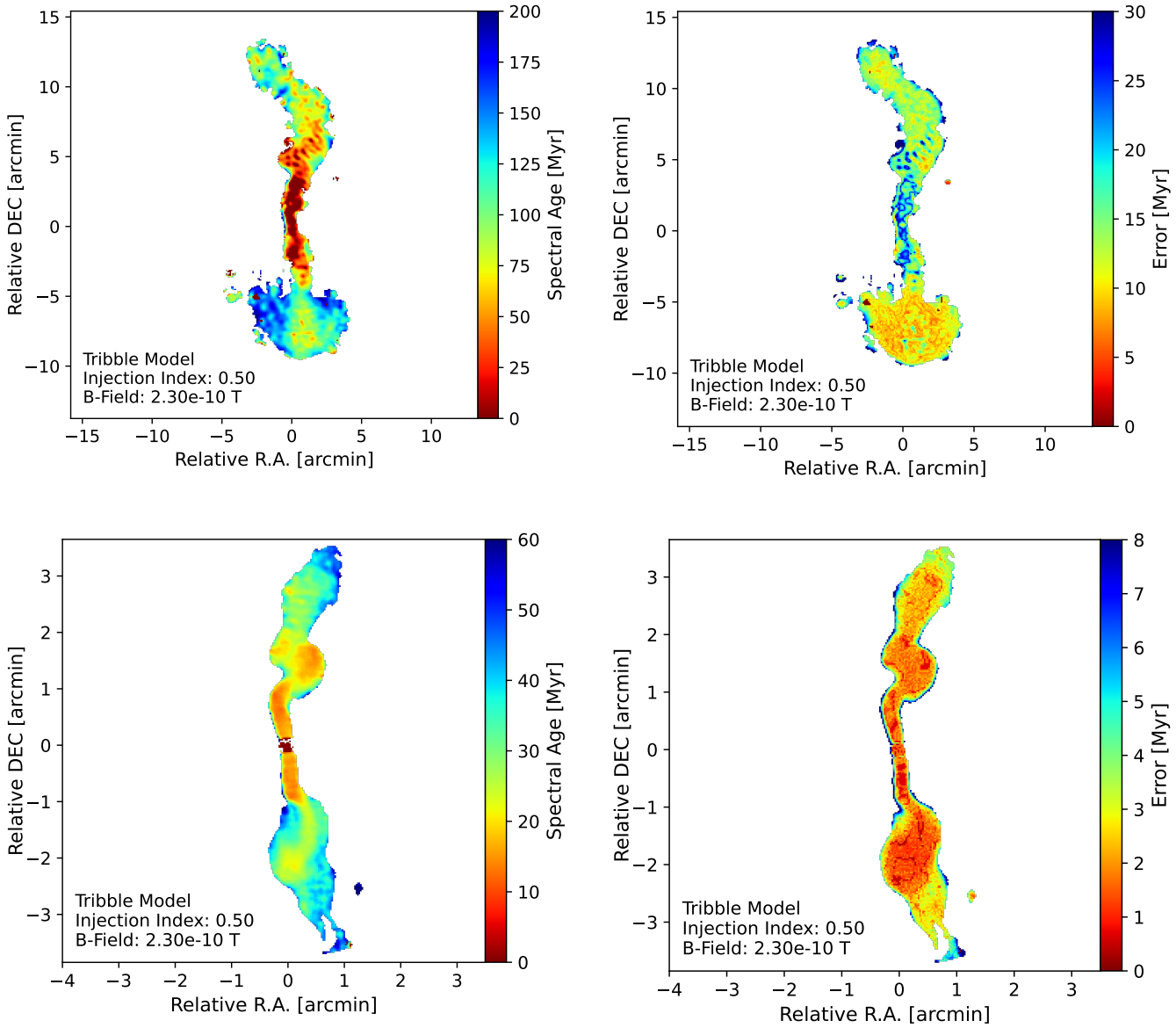

Fig. C.2. Spectral ageing maps obtained by fitting the Tribble model to the intensity maps, and corresponding maps of the uncertainty. Top-left panel: Map of the spectral age of 3C 449 between 145, 1365, and 1485 MHz, with the angular resolution of $20.0'' \times 20.0''$, by means of the BRATS software package. The parameters of the model are reported in the legend. Overall, the spectral age increases with the distance to the radio core. Top-right panel: Map of the upper error on the spectral age shown in the left panel. Bottom-left panel: Map of the spectral age of 3C 449 between 145, 1365, 4985, and 8485 MHz, with angular resolution of $6.0'' \times 6.0''$. Bottom-right panel: Map of the upper error on the spectral age shown in the left panel. In all the maps, the magnetic field intensity is $B = B_{\rm eq} = 2.3\,\mu$G.

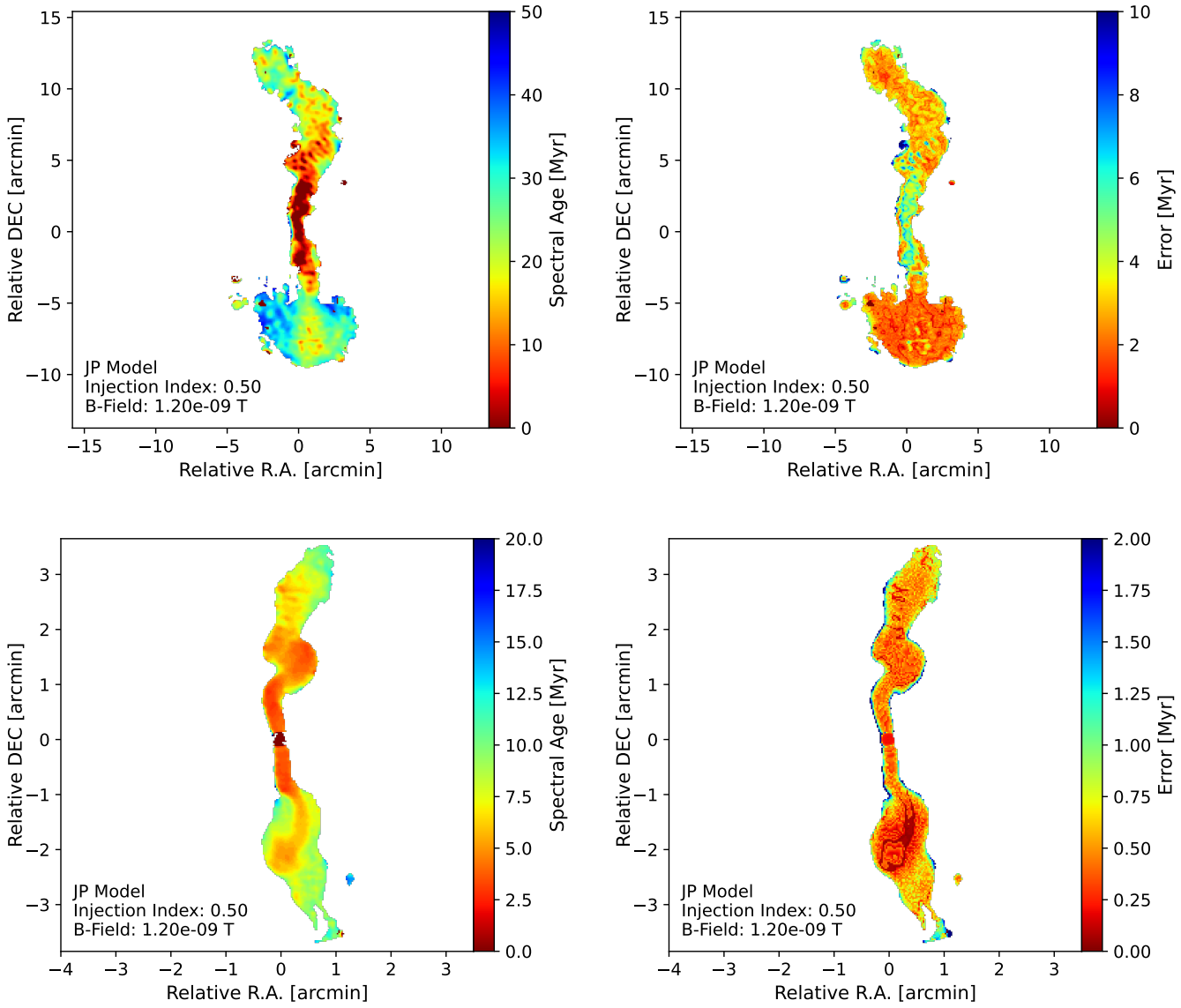

Fig. D.1. Spectral ageing maps obtained by fitting the JP model to the intensity maps, and corresponding maps of the uncertainty, using a magnetic field of $B = 12\mu$G. Top-left panel: Map of the spectral age of 3C 449 between 145, 1365, and 1485 MHz, with the angular resolution of $20.0'' \times 20.0''$. Top-right panel: Map of the upper error on the spectral age shown in the left panel. Bottom-left panel: Map of the spectral age of 3C 449 between 145, 1365, 4985, and 8485 MHz, with angular resolution of $6.0'' \times 6.0''$. Bottom-right panel: Map of the upper error on the spectral age shown in the left panel.